Research Article

Asra Anjum, Shaik Abdul Gaffar, Sateesh Kumar Deevi, Muhammad Faizan Ahmed, Umair Khan*, Taoufik Saidani*, Farhan Ali and Syed Sohaib Zafar

Numerical analysis of non-similar convection flows of a two-phase nanofluid past a semi-infinite vertical plate with thermal radiation

https://doi.org/10.1515/phys-2025-0232
Received February 1, 2025; accepted October 10, 2025;
published online December 3, 2025

Abstract: This research presents a computational investigation of non-linear, steady-state, incompressible laminar boundary-layer flow over a semi-infinite vertical plate using the Darcy–Forchheimer model along with Buongiorno's nanofluid model. Thermal convection and radiative heat and mass transfer of nanoparticles are considered. The research investigation fills a significant gap in the literature regarding the effects of Darcy–Forchheimer drag and heat radiation. The dimensionless nonlinear boundary value problem with associated wall and free stream boundary conditions is solved with the robust second-order accurate implicit finite-difference Keller Box technique to solve complex coupled nonlinear PDEs with high accuracy. The intricate interactions inside the fluid are clarified through extensive numerical simulations. An excellent correlation is obtained when our current code is validated using previous research from the literature, which had adopted numerous numerical techniques to solve the research problems. This study presents a novel non-similar analysis of two-phase nanofluid convection incorporating thermal radiation effects, which is rarely addressed in existing literature. The research uniquely captures the combined influence of Brownian motion, thermophoresis, and radiation on flow and heat transfer characteristics. The findings provide novel and creative insights into the structure of nanofluids in porous media, advancing our knowledge of fluid dynamics, heat, and mass transfer. It is observed that with increasing Darcy number (*Da*), there is a substantial increase in velocity, but temperature and concentration profiles decay; conversely, as Forchheimer number (*Fs*) enhances, velocity is depreciated; however, temperature and concentration profiles are elevated steadily. Moreover, increasing Brownian motion (*Nb*) enhances both velocity and temperature but reduces the concentration profile. Additionally, the velocity and temperature profiles are appreciated when thermal radiation (*R*) values are enhanced, but concentration decays. Temperature and velocity are reduced as the Prandtl number (*Pr*) increases, while concentration is elevated. Additionally, surface contour graphs and isothermal graphs are studied in detail. This current study has practical implications for enhancing the design and optimization of cooling systems, electronic thermal management, and energy systems, in circumstances where accurate control of temperatures and effective heat transmission are essential. By addressing the current research gap, this study makes major

***Corresponding authors: Umair Khan**, Department of Mathematics, Saveetha School of Engineering, Saveetha Institute of Medical and Technical Sciences, Saveetha University, Chennai 602105, Tamil Nadu, India; and Department of Mathematics, Faculty of Science, Sakarya University, Serdivan/Sakarya 54050, Turkey, E-mail: umairkhan@sakarya.edu.tr; and **Taoufik Saidani**, Center for Scientific Research and Entrepreneurship, Northern Border University, 73213, Arar, Saudi Arabia,
E-mail: Taoufik.Saidan@nbu.edu.sa
Asra Anjum and Shaik Abdul Gaffar, Sciences and Mathematics Unit, Department of Supportive Requirements, University of Technology and Applied Sciences, P.O. Box 608, PC:211, Salalah, Sultanate of Oman,
E-mail: Asra.Anjum@utas.edu.om (A. Anjum),
Abdulgaffar.Shaik@utas.edu.om (S. A. Gaffar).
https://orcid.org/0009-0002-7878-6798 (A. Anjum).
https://orcid.org/0000-0002-7368-1658 (S. A. Gaffar)
Sateesh Kumar Deevi, Department of Engineering Mathematics, Koneru Lakshmaiah Education Foundation, Guntur, Andhra Pradesh, 522302, India, E-mail: drsateeshdeevi@gmail.com.
https://orcid.org/0000-0001-8141-2899
Muhammad Faizan Ahmed and Farhan Ali, Department of Mathematical Sciences, Federal Urdu University of Arts, Sciences & Technology, Gulshan-e-Iqbal Karachi, 75300, Pakistan,
E-mail: mfaizanahmed@fuuast.edu.pk (M. F. Ahmed),
farhanali@fuuast.edu.pk (F. Ali).
https://orcid.org/0000-0002-6358-0407 (M. F. Ahmed)
Syed Sohaib Zafar, Department of Mathematics and Sciences, Sir Syed University of Engineering and Technology, Karachi, Pakistan,
E-mail: sohaib.zafar@ssuet.edu.pk.
https://orcid.org/0009-0006-1095-2314

advances in the fields of thermal sciences and nanofluid technology dynamics.

Keywords: nanofluids; non-similar solution; semi-infinite vertical plate; heat transfer; Brownian motion

Abbreviations

NPs	Nanoparticles
NF	Nanofluid
BNF	Buongiorno nanofluid
Da–*Fs*	Darcy–Forchheimer
R	Rosseland thermal radiation
BL	Boundary layer
BLT	Boundary layer thickness
BLEs	Boundary layer equations
BCs	Boundary conditions
BVP	Boundary value problem
KBM	Keller box method

Nomenclature

b	Inertial drag coefficient
C	Concentration
c_p	Specific heat parameter (J/kg K)
C_f	Skin friction coefficient
C_w	Concentration at the wall surface
C_∞	Ambient concentration
D	Nanoparticle diffusivity
Da	Darcy number
D_B	Brownian diffusion coefficient (m^2/s)
Dm	Molecular diffusivity (m^2/s)
D_T	Thermophoretic diffusion coefficient (m^2/s)
Fs	Forchheimer number
f	Non-dimensional steam function
g	Acceleration due to gravity (m/s^2)
Gr	Grashof number
K	Permeability
k_f	Thermal conductivity (W/mK)
α_f	Thermal diffusivity (m^2/s)
k^*	The mean absorption coefficient
L	Characteristic length (m)
Nb	Brownian motion parameter
Nt	Thermophoresis parameter
Nr	Buoyancy ratio parameter
Nu	Heat transfer rate (local Nusselt number)
p	Pressure (Pa)
Pr	Prandtl number
R	Radiation-conduction parameter
Sh	Mass transfer rate Sherwood number
Sc	Local Schmidt number
T	Temperature of the fluid (Kelvin)
T_w	Wall temperature (K)
T_∞	Ambient temperature (K)
x	Stream-wise coordinate (m)
y	Transverse coordinate (m)
V	Velocity field vector (m/s)
u, v	Non-dimensional velocity components along the x- and y-directions respectively (m/s)

Subscripts

w	Surface conditions
∞	Free stream conditions
q_r	Radiative heat flux

Greek symbols

α_f	Thermal diffusivity (m^2/s)
β	Volumetric volume expansion coefficient of the fluid (K)
σ_f	The electric conductivity of the fluid (S/m)
ρ_p	Fluid density of the nanoparticle
μ_f	Dynamic viscosity (kg m^{-1} s^{-1})
ν_f	Kinematic viscosity of base fluid (m^2/s)
τ	The ratio of heat capacity of the nanoparticle by the heat capacity of the fluid
$\sigma*$	Stefan-Boltzmann constant
θ	Dimensionless temperature
ϕ	Dimensionless concentration
ξ	Dimensionless tangential coordinate
η	Dimensionless radial coordinate
ψ	Dimensionless stream function
ρ_f	Density (kg/m^3)
$(\rho c_p)_p$	Heat capacity for the nanoparticles (J/kgK)

1 Introduction

Nanofluids (NFs) have gained recognition for superior thermophysical properties, enhancing heat transfer in applications compared to traditional fluids like water, ethylene glycol, and lubricants. Introduced by Choi [1], NFs improve cooling efficiency via dispersed nanoparticles (NPs). Researchers have explored various NP types (metal, oxides, carbides) in base fluids through simulations and experiments [2]. NFs are now used in engineering, medical services, food hygiene, aerodynamic cooling, atomic reactors, and solar collectors. They enhance fluids like propylene glycol and mineral oil with low heat conductivity. Nanotechnology enables tailoring NFs by adding specific NPs to meet advanced thermal requirements. Kuznetsov and Nield [3] analyzed nanofluid flow over smooth layers using the BNF model [4]. Ramesh Reddy et al. [5] examined Hall and ion-slip effects in NF transport. Razzaq et al. [6] explored Maxwell fluid flow in a magnetized sheet with NPs. Cui [7] investigated 3D bioconvective boundary layers with NPs and microorganisms. H. Pandharikar et al. [8] explored the numerical and experimental approaches to

evaluate nanoparticle-enhanced waste cooking oil biodiesel in a CI engine using a single-zone thermodynamic model. It revealed improved combustion efficiency, reduced emissions, and sustainable fuel performance with nanoparticle additives. Pandey et al. [9] studied the application of the inverse heat conduction algorithm to accurately estimate transient interfacial heat transfer coefficients between AZ31 alloy and H13 die during the casting process. A few more relevant works can be found in [10–13].

Buongiorno's nanofluid, engineered with enhanced heat transfer properties, improves efficiency in heat exchangers, auto-engines, and electronic cooling systems. Blending base fluids with nanoparticles (NPs) it enhances convection heat transfer and thermal conductivity, offering compact and efficient solutions for engineering applications. The Buongiorno nanofluid model incorporates thermal analysis and Brownian motion of fluid particles. Rasheed et al. [14] modelled two-dimensional magneto NFs with convective fluxes using the BVPh2 algorithm, considering heat absorption and generation. Bhavani [15] examined stable, ultrafast nano-coolants suitable for non-radiative designs. Humane et al. [16] studied magneto-micropolar NFs in porous, stretchable devices. Wang et al. [17] used a modified Buongiorno model to analyze $Ag-H_2O$ nano-thin film heat transfer in permeable media. Rafique et al. [18] examined the combined effects of Brownian motion, thermophoretic diffusion, and the Soret and Dufour phenomena on micropolar nanofluid flow over an inclined sheet using Keller-box simulations to enhance the modeling of thermal and diffusive transport. Shahbaz et al. [19] employed an advanced intelligent computational framework to examine three-dimensional thermally laminated magnetohydrodynamic flow of non-Newtonian nanofluids over a stretched surface and demonstrated improved accuracy in predicting thermal and fluid dynamic characteristics.

Non-similar transformations are mathematical tools used to analyze fluid flows where variables like velocity, temperature, or concentration do not maintain similarity across the flow field. These techniques introduce new variables to address non-uniform boundary conditions, geometries, or varying parameters, enabling the resolution of complex fluid dynamics problems. Non-similar flows arise when material properties depend on independent variables, preventing a unified dimensionless form. These transformations are vital for modelling real-world scenarios like varying freestream speeds, temperature differences, fluid injection, or surface mass transfer. Non-similar flows differ from similar ones along the streamwise direction. Techniques such as the LNS method, developed by Sparrow et al. [20], have been widely adopted to address non-similar boundary layer (BL) problems. Razzaq and Farooq [21] used non-similar forced convection to study Oldroyd-B fluid flow over an exponentially stretching substrate. Abdullah et al. [22] analyzed the effects of Brownian motion, thermophoresis, and mixed convection on nanofluid flow near a heated vertical surface. Anjum et al. [23] employed non-similar transformations and demonstrated that the inclusion of Ohmic heating and viscous dissipation notably improved thermal transfer performance and modified the flow behavior in the magneto-thermo-convective motion of nanofluids along a semi-infinite vertical surface.

Convection flows are fluid movements driven by density and temperature variations, where the process of convection, cooler, denser fluid sinks, while warmer than usual, less dense fluid ascends. These flows transfer heat within fluids and are critical in atmospheric circulation, ocean currents, and engineering systems like HVAC and cooking appliances. Natural convection, driven by density fluctuations and gravity, contrasts with forced convection, initiated by external sources like pumps or fans. Mixed convection combines both effects [24, 25]. In mechanical and petroleum-related engineering, convection fluxes in porous media are used in increased extraction of oil, geothermal power, and nuclear management of waste.

The Darcy number is a dimensionless measure representing fluid flow through porous media, named after Henry Darcy, who pioneered studies in porous media fluid dynamics. It is defined as the proportion of permeability to a characteristic length squared. The Forchheimer number, another dimensionless parameter, describes the significance of viscous forces relative to inertial forces in porous media and is used in analyzing flows through materials like packed beds and filters. Porous media, with voids or pores, can be natural (e.g., sandstone, human skin) or synthetic, tailored for industrial applications. Porosity is the proportion of the entire volume compared to pore volume. These media play vital roles in manufacturing, drug purification, water filtration, engineering construction, and packed bed reactors for heat and mass transfer. Darcy's law links fluid flow to the Earth's gravity and stress gradients in porous media. Larger pores increase porosity, enhancing flow but expanding viscous shear resistance. P. Forchheimer [26] modified Darcy's law in 1901 by introducing a velocity-squared term to account for inertial forces, forming the Forchheimer number, further refined by Muskat [27] as the "Forchheimer term." Ganesh et al. [28] noted increased temperature with viscous effects in magnetohydrodynamics. Makinde et al. [29] studied in a (*Da-Fs*) porous medium, fractional dynamics of entropy generation in unstable convection and

conduction of a reactive nanofluid across a slippery, porous sheet, making porous media critical in engineering and manufacturing.

Thermal radiation involves heat energy release via electromagnetic waves due to temperature, primarily in the infrared range. Governed by Planck's law, Stefan–Boltzmann law, and Wien's displacement law, it significantly affects energy balance and heat transport in fluid systems, particularly at high temperatures. It interacts with conduction and convection in fields like atmospheric science, astrophysics, and thermal engineering. High-temperature engineering must account for thermal radiation's impact on heat flow, as seen in industrial applications. Tunde et al. [30] used homotopy analysis for second-grade radiative MHD flows on surfaces. Jawad et al. [31] examined MHD hybrid nanofluid flow with heat radiation on expanding/contracting surfaces. Jile et al. [32] explored Maxwell nanofluid flows with Dufour, Soret, and thermal conductivity effects. Modifications in waste discharge concentration and the presence of quadratic thermal radiation significantly impacted the fluid flow behaviour and heat transfer of an oblique stagnation point Boger HNF over a cylindrical surface, as shown by Madhu et al. [33]. The Levenberg–Marquardt backpropagation neural network demonstrated by Raja et al. [34] effectively represented the effects of Hall currents and thermal radiation on the boundary layer flow past a stretching sheet, guaranteeing enhanced analytical precision and efficiency.

A semi-infinite vertical plate is an idealized model extending infinitely in height and one horizontal direction, simplifying the study of natural convection and boundary layer (BL) patterns by eliminating edge effects. This model aids in analyzing mass and heat transfer in buoyancy-driven flows relevant to heat exchangers, electronic cooling, building ventilation, pollutant dispersion, and oceanic thermal plumes. H. Pohlhausen [35] first used the momentum integral approach to study convection near a semi-infinite plate. S. Ostrach [36] introduced similarity solutions for free convection flows, solving coupled nonlinear ODEs using air as the fluid. B. Gebhart et al. [37] documented studies on convection with air or water, addressing the mass transfer effects of dissolved materials. B. Gebhart and L. Pera [38] developed the parameter (*Nr*) to relate flow density variations to chemical and heat diffusion. Amanullah et al. [39] explored non-Newtonian Nanofluid flow over a semi-infinite vertical surface with slip effects. Chamkha et al. [40] analyzed mass and heat transfer with magnetic conduction over a porous substrate. Gangadhar et al. [41] explored radiative second-grade nanofluid (NF) flows via a modified BNF model across a Riga plate with convective heating. Under various circumstances, many studies have been done on semi-infinite plates with myriad effects [42–45].

In the present work, a mathematical model is developed for steady-state laminar boundary layer flow of a Buongiorno nanofluid past a semi-infinite vertical plate with the Darcy–Forchheimer (*Da*–*Fs*) model, with heat radiation impacts, unlike previous studies which focused on either the (*Da*–*Fs*) or Buongiorno's model individually and have been confined to ordinary differential equations. The article fills a critical research gap by integrating the (*Da*–*Fs*) model with BNF theory and thermal radiation to study non-similar convection flows. The novelties of the current work are the simultaneous consideration of the combined effects of Darcy–Forchheimer drag and Buongiorno's nanofluid model with radiation on non-similar convection flows past a semi-infinite vertical plate and ODEs which include fully two-dimensional NF flow. Moreover, velocity, temperature, concentration profiles, surface and contour graphs, and isothermal graphs are studied in detail. These have not been considered in previous studies. The dimensionless nonlinear multi-physical BVP with related wall and free stream BCs is solved using the robust 2nd order accurate implicit KBM. Validation using previous special instances that have been documented in the literature and authentication is also accomplished. Velocity, temperature, and concentration distributions are computed and visualized graphically for the influence of (*Nb*), (*Nt*), (*Nr*), (*Da*), (*Fs*), (*R*), (*Pr*), (*Sc*), (*Gr*). Additionally, graphs and tabular form for (C_f), (*Sh*), (*Nu*), for parameters are also shown *for R*, *Pr*, *Sc*, *Da*, *and Fs*. The simulations are relevant and provide an in-depth parametric study, investigating the impact of various factors like permeability, porosity, nanoparticle volume fraction, and thermal conductivity on motion and heat transfer. The article's findings can be used in the design and optimization of heating and cooling systems, and energy systems by providing accurate predictions of heat, mass transmission, and fluid flow patterns.

2 Mathematical analysis

A laminar, steady-state, incompressible convection flow of NF past a semi-infinite plate in an (*x*, *y*) coordinate system is studied, as illustrated in Figure 1a. Whereas, vertical plate is followed by the *x*-axis going higher, and the *y*-axis going normal to the plate. Buoyancy effects are often caused by gradients in a dispersed species' thermal region, which drives the flow. The flow over the horizontal sheet described by Navier–Stokes becomes identical to boundary-layer equations as the characteristic value of natural convection, or the Grashof number (*Gr*), is increased indefinitely.

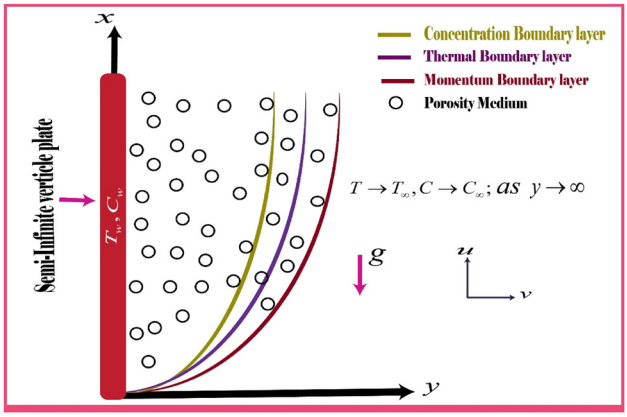

Figure 1a: Flow geometry of the problem.

Gravitational acceleration (g) exerts a downward force. Both NF and semi-infinite plates are first kept constant in terms of both temperature and concentration. Additionally, the temperature and concentration at the wall surface are higher than the constant free stream temperature and concentration $T_w > T_\infty$, and $C_w > C_\infty$, respectively.

The current flow assumption can be described as follows:

- Darcy–Forchheimer flow has been used to examine the porous flow in the Buongiorno nanofluid model in the momentum equation.
- The Rosseland approximation for thermal convection has been used in the energy condition.

To approximate the conductivity, a homogeneous and isotropic porous medium is considered. The second-order (Da–Fs) model's pressure gradient is described in the following way:

$$\nabla_p = -aU + bU^2 \tag{1}$$

where ∇_p is the pressure, $a = \frac{\mu}{K}$ and $b = \frac{\rho}{K_1}$ are the constants, and U is the velocity. The governing equations for mass, momentum, energy, and nanoparticle species (concentration) for the BNF under the BL and Boussinesq approximations may be established using the models of Buongiorno [4], Ramesh Reddy et al. [5], and Anjum et al. [23, 46]. The vectorial forms of the conservation equations are:

$$\nabla \cdot \boldsymbol{V} = 0 \tag{2}$$

$$\rho_f\left(\frac{\partial \boldsymbol{V}}{\partial t} + \boldsymbol{V}\cdot\nabla\boldsymbol{V}\right) = -\nabla p + \mu_f(\nabla^2\boldsymbol{V}) + g\left[(1-C_\infty)\rho_{f\infty}(T-T_\infty)\times\beta - (\rho_p-\rho_{f\infty})(C-C_\infty)\right] - \frac{\upsilon_f}{K}\boldsymbol{V} - \frac{b}{K}\boldsymbol{V}^2 \tag{3}$$

$$(\rho c_p)_f\left(\frac{\partial T}{\partial t} + \boldsymbol{V}\cdot\nabla T\right) = k_f\nabla^2 T + (\rho c_p)_p\left[D_B\nabla C\cdot\nabla T + \frac{D_T}{T_\infty}(\nabla T)^2\right] - \frac{\partial q_r}{\partial y} \tag{4}$$

$$\frac{\partial C}{\partial t} + \boldsymbol{V}\cdot\nabla C = D_m\nabla^2 C + \frac{D_T}{T_\infty}\nabla^2 T \tag{5}$$

The radiative flux is expressed via the Rosseland approximation [47–50] as follows:

$$q_r = -\frac{4\sigma^*}{3k^*}\frac{\partial T^4}{\partial y} \tag{6}$$

Furthermore, T^4 can be simplified using the Taylor series at about T_∞, and ignoring the higher order, we get [49]:

$$T^4 \cong 4T_\infty^3 T - 3T_\infty^4. \tag{7}$$

Thus, Eq. (6) becomes:

$$q_r = -\frac{16\sigma^* T_\infty^3}{3k^*}\frac{\partial T}{\partial y} \tag{8}$$

Using (8) and (9), we get:

$$\frac{\partial q_r}{\partial y} = \frac{-16\sigma^* T_\infty^3}{3k^*}\frac{\partial^2 T}{\partial y^2} \tag{9}$$

The semi-infinite substrate surface (wall) and free stream (BL edge) are subject to the following boundary conditions, Anjum et al. [23, 46]:

$$\begin{aligned} u = \upsilon = 0, \quad T = T_w, \quad C = C_w \quad \text{at} \quad y = 0 \\ u \to 0, \quad T \to T_\infty, \quad C \to C_\infty \quad \text{as} \quad y \to \infty \end{aligned} \tag{10}$$

Given the low concentration of nanoparticles and the use of an appropriate pressure option, in line with Kuznetsov and Nield [3], Eq. (3) can be written with the Oberbeck–Boussinesq approximation, yielding the linearized momentum equation, which is as follows:

$$0 = -\nabla p + \mu_f(\nabla^2\boldsymbol{V}) + g\left[(1-C_\infty)\rho_{f\infty}\beta(T-T_\infty) - (\rho_p-\rho_{f\infty})(C-C_\infty)\right] - \frac{\upsilon_f}{K}\boldsymbol{V} - \frac{b}{K}\boldsymbol{V}^2 \tag{11}$$

The reduced BL conservation equations in an (x, y) coordinate system for the steady flow are as follows:

$$\frac{\partial u}{\partial x} + \frac{\partial \upsilon}{\partial y} = 0 \tag{12}$$

$$u\frac{\partial u}{\partial x} + \upsilon\frac{\partial u}{\partial y} = \upsilon_f\frac{\partial^2 u}{\partial y^2} + g\left[(1-C_\infty)\rho_{f\infty}\beta(T-T_\infty) - (\rho_p-\rho_{f\infty})(C-C_\infty)\right] - \frac{\upsilon_f}{K}u - \frac{b}{K}u^2 \tag{13}$$

$$u\frac{\partial T}{\partial x}+\upsilon\frac{\partial T}{\partial y}=\alpha_f\frac{\partial^2 T}{\partial y^2}+\tau\left[D_B\frac{\partial T}{\partial y}\frac{\partial C}{\partial y}+\frac{D_T}{T_\infty}\left(\frac{\partial T}{\partial y}\right)^2\right]+\frac{1}{(\rho c_p)_f}\frac{16\sigma^* T_\infty^3}{3k^*}\frac{\partial^2 T}{\partial y^2} \tag{14}$$

$$u\frac{\partial C}{\partial x}+\upsilon\frac{\partial C}{\partial y}=D_m\frac{\partial^2 C}{\partial y^2}+\frac{D_T}{T_\infty}\frac{\partial^2 T}{\partial y^2} \tag{15}$$

where:

$$\alpha_f=\frac{k_f}{(\rho c)_f},\qquad \tau=\frac{(\rho c_p)_p}{(\rho c_p)_f}. \tag{16}$$

In addition, the stream function ψ are defined as $u=\frac{\partial\psi}{\partial y}$ and $\upsilon=-\frac{\partial\psi}{\partial x}$. Equation (12) is automatically satisfied subject to the velocity components expressed in terms of the stream function. Also, the following non-dimensional scaling variables are introduced (see Ramesh Reddy et al. [5] and Anjum et al. [23, 46]):

$$\xi=\left(\frac{x}{L}\right)^{\frac{1}{2}},\qquad \eta=C_1 y x^{-\frac{1}{4}},\qquad \psi=4\upsilon_f C_1 x^{\frac{3}{4}} f(\xi,\eta),$$
$$C_1=\left(\frac{Gr}{4}\right)^{\frac{1}{4}}L^{\frac{-3}{4}}$$
$$Gr=\frac{g\beta(1-C_\infty)\rho_{f\infty}(T_w-T_\infty)L^3}{4\upsilon_f^2},$$
$$\theta(\xi,\eta)=\frac{T-T_\infty}{T_w-T_\infty},\qquad \phi(\xi,\eta)=\frac{C-C_\infty}{C_w-C_\infty} \tag{17}$$

In addition, Eqs. (13)–(15) are thereby rendered into the following coupled nonlinear ODEs by virtue of the transformations in Eq. (17):

$$f'''+3ff''-2f'^2+(\theta-Nr\phi)-\frac{\xi}{Da\,Gr^{\frac{1}{2}}}f'-\frac{Fs}{Da}\xi^2 f'^2=2\xi\left(f'\frac{\partial f'}{\partial\xi}-f''\frac{\partial f}{\partial\xi}\right) \tag{18}$$

$$\frac{\theta''}{Pr}(1+R)+3f\theta'+Nb\,\theta'\phi'+Nt\,\theta'^2=2\xi\left(f'\frac{\partial\theta}{\partial\xi}-\theta'\frac{\partial f}{\partial\xi}\right) \tag{19}$$

$$\frac{\phi''}{Sc}+3f\phi'+\frac{1}{Sc}\frac{Nt}{Nb}\theta''=2\xi\left(f'\frac{\partial\phi}{\partial\xi}-\phi'\frac{\partial f}{\partial\xi}\right) \tag{20}$$

The transformed non-dimensional boundary conditions are:

$$f=0,\quad f'=0,\quad \theta=1,\quad \phi=1\qquad \text{at}\quad \eta=0$$
$$f'\to 0,\quad \theta\to 0,\quad \phi\to 0\quad \text{as}\quad \eta\to\infty. \tag{21}$$

In which

$$Nb=\frac{\tau D_B(C_w-C_\infty)}{\upsilon_f},\quad Nt=\frac{\tau D_T(T_w-T_\infty)}{\upsilon_f T_\infty},$$
$$Nr=\frac{(\rho_p-\rho_{f\infty})(C_w-C_\infty)}{\rho_{f\infty}(1-C_\infty)\beta(T_w-T_\infty)}$$
$$Da=\frac{K}{2L^2},\quad Fs=\frac{2b}{L},\quad Pr=\frac{\upsilon_f}{\alpha_f},\quad Sc=\frac{\upsilon_f}{D_m},\quad R=\frac{16\sigma^* T_\infty^3}{3k_f k^*}. \tag{22}$$

The above equations comprised distinct dimensionless influential parameters which are mathematically expressed in equation (22). Namely these parameters along with the other mathematical symbols or notations used in the paper are given in the nomenclature.

The shear stress components at the surface, known as the skin-friction coefficients (C_f), the heat transfer rate known as the Nusselt number (Nu), and the mass transfer rate of NPs, known as the Sherwood number (Sh), are the physically key interesting engineering design parameters for the existing semi-infinite vertical surface. They are defined as follows:

$$\frac{1}{4\upsilon_f\mu C_1{}^3 x^{\frac{1}{4}}}C_f=f''(\xi,0) \tag{23}$$

$$\frac{-1}{k_f\Delta T C_1 x^{\frac{-1}{4}}}Nu=\theta'(\xi,0) \tag{24}$$

$$\frac{-1}{D_m\Delta C\,C_1 x^{\frac{-1}{4}}}Sh=\phi'(\xi,0) \tag{25}$$

where $\Delta T=T_w-T_\infty$, and $\Delta C=C_w-C_\infty$. Also, if $\xi\sim 0$ then the BLEs (18)–(20) changed to the following similarity ODEs:

$$f'''+3ff''-2f'^2+\theta-Nr\phi=0, \tag{26}$$

$$\frac{\theta''}{Pr}(1+R)+3f\theta'+Nb\,\theta'\phi'+Nt\,\theta^2=0, \tag{27}$$

$$\frac{\phi''}{Sc}+3f\phi'+\frac{1}{Sc}\frac{Nt}{Nb}\theta''=0. \tag{28}$$

3 Methodology

The Keller box implicit finite difference scheme [51] has been applied to numerically solve the dimensionless boundary layer equations (18)–(20). This method remains one of the most influential numerical schemes for solving two-point BVPs. The Keller-box approach offers appealing extrapolation properties and second-order accuracy with flexible spacing. On a rectangular grid Figure 1b, a finite-difference technique is used (box) and converts the

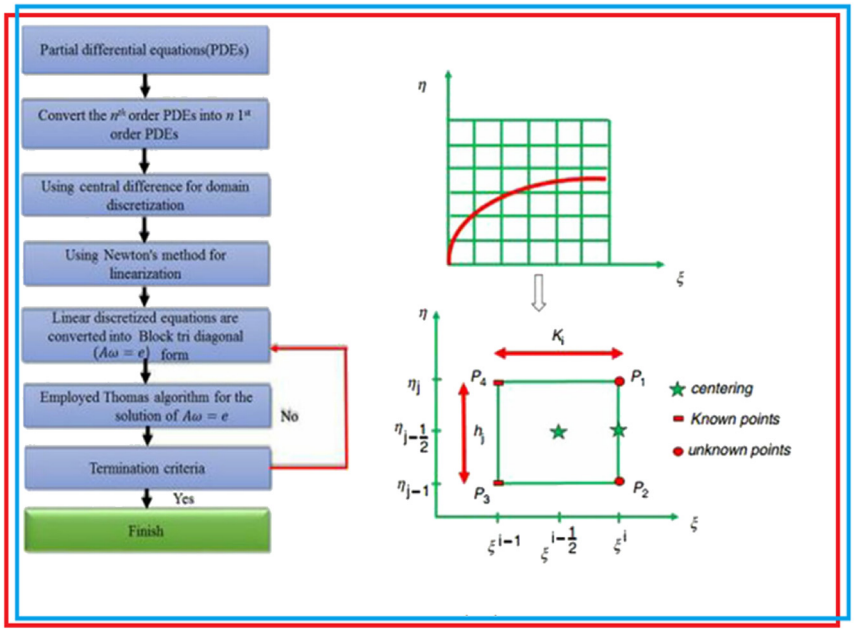

Figure 1b: Keller box procedure, box cell, and boundary layer meshing.

partial differential equations of BL into an algebraic set of equations. It attains remarkable accuracy, offers steady numerical meshing characteristics, and converges quickly. By utilizing fully implicit methods with customizable stepping, the Keller box approach improves accuracy on explicit or semi-implicit schemes. Another advantage of this KBM is that the non-similar solutions can be easily obtained via this scheme as compared to other numerical approaches. In line with the physics of parabolic systems, each discretization step is fully coupled.

The discrete algebra connected to the KBM is essentially independent of any other mimicking (physics-capturing) computation methods [52–54].

The four phases involved in the KBM are:

(1) splitting the system of Nth order PDEs down to *the N first-order* ODEs,
(2) finite difference discretization,
(3) quasi-linearization of non-linear Keller algebraic equations,
(4) block-tridiagonal elimination solution of the linearized Keller algebraic equations.

Step 1: Reduction of the Nth order partial differential equation system to N first-order equations.

Equations (18)–(21), together with new variables, are used to transform the boundary value problem into a multiple system of 1st order equations. Thus, adding the new variables results in a set of nine simultaneous first-order ODEs:

$$u(x,y) = f', \quad v(x,y) = f'', \quad g'(x,y) = p, \quad s(x,y) = \theta, \quad t(x,y) = \theta' \tag{29}$$

$$f' = u \tag{30}$$

$$u' = v \tag{31}$$

$$g' = p \tag{32}$$

$$s' = t \tag{33}$$

$$v' + 3fv - 2u^2 + (s - Nr\, g) - \frac{\xi}{Da\sqrt{Gr}}(u) - \frac{Fs}{Da}\xi^2 u^2 = 2\xi\left[u\frac{\partial u}{\partial \xi} - v\frac{\partial f}{\partial \xi}\right] \tag{34}$$

$$\frac{t'}{Pr}(1+R) + 3ft + Nb\, t\, p + Nt\, t^2 = 2\xi\left(u\frac{\partial s}{\partial \xi} - t\frac{\partial f}{\partial \xi}\right) \tag{35}$$

$$\frac{p'}{Sc} + 3fp + \frac{1}{Sc}\frac{Nt}{Nb}t' = 2\xi\left(u\frac{\partial g}{\partial \xi} - p\frac{\partial f}{\partial \xi}\right) \tag{36}$$

where primes denote differentiation with respect to η. In terms of the dependent variables, the BCs become:

$$f = 0, \quad f' = 0, \quad \theta = 1, \quad \phi = 1 \quad \text{at} \quad \eta = 0$$
$$f' \to 1, \quad \theta \to 0, \quad \phi \to 0 \quad \text{as} \quad \eta \to \infty \tag{37}$$

Step 2: Finite difference discretization

In a Keller box (cell), a 2D computational grid is imposed in the ξ–η plane. The stepping process is defined by:

$$\eta_0 = 0,\ \ \eta_j = \eta_{j-1} + h_j,\ \ j = 1, 2, \ldots, J,\ \ \eta_J \equiv \eta_\infty \tag{38}$$

$$\xi^0 = 0, \qquad \xi^n = \xi^{n-1} + k_n, \quad n = 1, 2, \ldots, N \tag{39}$$

where k_n is the $\Delta\xi$ – spacing and h_j is the $\Delta\eta$ – spacing. If g_j^n denotes the value of any variable at (η_j, ξ^n), then the variables and derivatives of Eqs. (29)–(36) at $(\eta_{j-1/2}, \xi^{n-1/2})$ are replaced by:

$$g_{j-1/2}^{n-1/2} = \frac{1}{4}\left(g_j^n + g_{j-1}^n + g_j^{n-1} + g_{j-1}^{n-1}\right) \tag{40}$$

$$\left(\frac{\partial g}{\partial \eta}\right)_{j-1/2}^{n-1/2} = \frac{1}{2h_j}\left(g_j^n - g_{j-1}^n + g_j^{n-1} - g_{j-1}^{n-1}\right) \tag{41}$$

$$\left(\frac{\partial g}{\partial \xi}\right)_{j-1/2}^{n-1/2} = \frac{1}{2k^n}\left(g_j^n - g_{j-1}^n + g_j^{n-1} - g_{j-1}^{n-1}\right) \tag{42}$$

The resulting finite-difference approximation of Equations (29)–(36) for the mid-point $(\eta_{j-1/2}, \xi^n)$, are:

$$h_j^{-1}\left(f_j^n - f_{j-1}^n\right) = u_{j-1/2}^n \tag{43}$$

$$h_j^{-1}\left(u_j^n - u_{j-1}^n\right) = v_{j-1/2}^n \tag{44}$$

$$h_j^{-1}\left(g_j^n - g_{j-1}^n\right) = p_{j-1/2}^n \tag{45}$$

$$h_j^{-1}\left(s_j^n - s_{j-1}^n\right) = t_{j-1/2}^n \tag{46}$$

$$\begin{aligned}
&(v_j - v_{j-1}) + \frac{h_j}{4}(3+2\alpha)(f_j + f_{j-1})(v_j + v_{j-1}) \\
&\quad + \frac{h_j}{2}(s_j + s_{j-1} - Nr(g_j + g_{j-1})) \\
&\quad - 2\left(1 + \alpha - \frac{Fs}{Da}\xi^2\right)\frac{h_j}{4}(u_j + u_{j-1})^2 \\
&\quad - \frac{\xi}{Da\sqrt{Gr}}\frac{h_j}{2}(u_j + u_{j-1}) \\
&\quad - \alpha h_j f_{j-1/2}^{n-1}(v_j + v_{j-1}) - \alpha h_j v_{j-1/2}^{n-1} \\
&\quad \times (f_j + f_{j-1}) - v^{n-1} = [R_1]_{j-/12}^{n-1}
\end{aligned} \tag{47}$$

$$\begin{aligned}
&\frac{1}{\mathrm{Pr}}(1+R)(t_j - t_{j-1}) + \frac{h_j}{4}(3+2\alpha)(f_j + f_{j-1})(t_j + t_{j-1}) \\
&\quad + Nb\frac{h_j}{4}(t_j + t_{j-1})(p_j + p_{j-1}) \ + Nt\frac{h_j}{4}(t_j + t_{j-1})^2 \\
&\quad - 2\frac{\alpha h_j}{4}(su)_{j-1/2}^{n-1} + \alpha h_j \\
&\quad \times \begin{pmatrix} s_{j-1/2}^{n-1}(u_j + u_{j-1}) - u_{j-1/2}^{n-1}(s_j + s_{j-1}) \\ -f_{j-1/2}^{n-1}(t_j + t_{j-1}) + t_{j-1/2}^{n-1}(f_j + f_{j-1}) \end{pmatrix} \\
&\quad = [R_2]_{j-1/2}^{n-1}
\end{aligned} \tag{48}$$

$$\begin{aligned}
&\frac{1}{Sc}(p_j - p_{j-1}) + \frac{1}{Sc}\frac{Nt}{Nb}(t_j - t_{j-1}) + \frac{h_j}{4}(3+2\alpha) \\
&\quad \times (f_j + f_{j-1})(p_j + p_{j-1}) \\
&\quad - 2\frac{\alpha h_j}{4}(ug)_{j-1/2}^{n-1} + 2\frac{\alpha h_j}{2} \\
&\quad \times \begin{pmatrix} g_{j-1/2}^{n-1}(u_j + u_{j-1}) - u_{j-1/2}^{n-1}(g_j + g_{j-1}) \\ -f_{j-1/2}^{n-1}(p_j + p_{j-1}) + p_{j-1/2}^{n-1}(f_j + f_{j-1}) \end{pmatrix} \\
&\quad = [R_3]_{j-1/2}^{n-1}
\end{aligned} \tag{49}$$

Where:

$$\begin{aligned}
[R_1]_{j-1/2}^{n-1} = -h_j\Big[&(v')_{j-1/2}^{n-1} + (3-2\alpha)(f\ v)_{j-1/2}^{n-1} \\
&+ \left(s_{j-1}^{n-1} - Nr\ g_{j-1}^{n-1}\right) - \frac{.\xi}{Da\sqrt{Gr}}\left(u_{j-1}^{n-1}\right) \\
&+ \left(2 - 2\alpha - \frac{Fs}{Da}\right)\left(u_{j-1}^{n-1}\right)^2\Big]
\end{aligned} \tag{50}$$

$$\begin{aligned}
[R_2]_{j-1/2}^{n-1} = -h_j\Big[&\frac{1}{\mathrm{Pr}}(1+R)(t')_{j-1/2}^{n-1} + (3-2\alpha)(ft)_{j-1/2}^{n-1} \\
&+ Nb(tp)_{j-1/2}^{n-1} + Nt(t^2)_{j-1/2}^{n-1} + 2\alpha(us)_{j-1/2}^{n-1}\Big]
\end{aligned} \tag{51}$$

$$\begin{aligned}
[R_3]_{j-1/2}^{n-1} = -h_j\Big[&\frac{1}{Sc}(p')_{j-1/2}^{n-1} + \frac{1}{Sc}\frac{Nt}{Nb}(t')_{j-1/2}^{n-1} \\
&+ (3-2\alpha)(fp)_{j-1/2}^{n-1} + 2\alpha(ug)_{j-1/2}^{n-1}\Big]
\end{aligned} \tag{52}$$

The boundary conditions are:

$$\begin{aligned}
&f_0^n = 0, \quad u_0^n = 0, \quad g_0^n = 0, \quad s_0^n = 0, \quad u_J^n = 0, \\
&g_J^n = 0, \quad s_J^n = 0
\end{aligned} \tag{53}$$

Stage 3: Quasi-linearization of non-linear Keller algebraic equations

If we assume $f_j^{n-1}, u_j^{n-1}, v_j^{n-1}, g_j^{n-1}, p_j^{n-1}, s_j^{n-1}, t_j^{n-1}$ to be known for $0 \le j \le J$. This leads to a system of $7J + 7$ equations for the solution of $7J + 7$ unknowns $f_j^n, u_j^n, v_j^n, g_j^n, p_j^n, s_j^n, t_j^n j = 0, 1, 2, \ldots, J$. This non-linear system of algebraic equations is linearized using Newton's method.

Stage 4: Block-tridiagonal elimination solution of linear Keller algebraic equations

The linearized system has a block-tridiagonal structure, and hence the block-elimination approach is used to solve this system. Block matrices make up the produced block-tridiagonal layout. The entire linearized system is expressed as a block matrix system, in which every element of the coefficient matrix is a matrix in and of itself. The effective

Keller-box method is used to solve this system. The number of mesh points in both directions has a big impact on the numerical output. Following a few trials, a greater number of mesh points are chosen in the η-direction (radial coordinate), whereas a much smaller number of mesh points are used in the ξ-direction (tangential coordinate). $\eta_{\max} = 14$ defines a sufficiently large value at which the specified BCs are accomplished. For this flow domain, $\xi_{\max}$ is set as 3. In the current computation, mesh independence is attained. The computational algorithm is run on a PC using MATLAB. As explained by Keller [51], the procedure exhibits outstanding stability, convergence, and consistency.

3.1 Convergence analysis

Until a certain convergence threshold is met, computations are performed. The wall shear stress parameter, v (ξ, 0), is frequently employed as the convergence criterion in laminar BL computations [55]. It is discovered that the wall shear stress parameter is typically exhibit the largest inaccuracy due to the BL computation. Notably, this convergence criterion is applied throughout the investigation since it is effective, appropriate, and the best solution to all of the difficulties explored. Calculations are halted if $\left|\delta v_0^{(i)}\right| \prec \varepsilon_1$, where ε_1 is a small, prescribed value.

3.2 Validation of the scheme

The Nusselt number (*Nu*) for *Pr* values is compared to those published in previous studies to assess the validity of the present numerical code. Table 1, exhibited by comparing the validity of the current research to previous investigations by Amanullah et al. [39], utilized the KBM method in their research, and Chamkha and Aly [40] used the iterative, tri-diagonal, implicit finite-difference method. Based on the most recent results, very close agreement is achieved, confirming the accuracy of the present Keller box code. Strong agreement and reliability in the observed trends are indicated by the data, which indicates that the current results support and reinforce the findings of earlier investigations. Error analysis percentages of the comparisons are also included. Tables 2 and 3 validate the current research with Rao et al. [43], who employed the finite element technique in their studies, and Gaffar et al. [44], who employed the KBM technique.

Table 1: Comparison of Nusselt number (*Nu*) for different *Pr* values.

Pr	Nusselt Number (*Nu*)				
	Amanullah et al. [39] (KBM)	Chamkha and Aly [40] (iterative, tri-diagonal, implicit finite-difference method)	Present results	Error analysis (%) with [39]	Error analysis (%) with [40]
1	0.40181	0.40178	0.40179	2 %	1 %
10	0.4656	0.4658	0.4657	1 %	1 %
100	0.49066	0.49063	0.49064	2 %	1 %
1,000	0.49742	0.49739	0.49741	2 %	2 %

Table 2: Comparison of values of C_f and *Nu* for different values of *R* when $Pr = 0.71$.

R	Rao et al. [43] (finite element technique)		Gaffar et al. [44] (KBM)		Present results for (KBM)	
	C_f	*Nu*	C_f	*Nu*	C_f	*Nu*
0.0	2.1664	0.8365	2.1665	0.8364	2.1659	0.8366
0.5	2.4657	0.6139	2.4656	0.6140	2.4659	0.6142
1.0	2.6546	0.5032	2.6547	0.5031	2.6549	0.5035
2.0	2.9039	0.4010	2.9038	0.4011	2.9041	0.4013

Table 3: Comparison of values of C_f and *Sh* for different values of *Sc* when $Pr = 0.71$.

Sc	Rao et al. [43] (finite element technique)		Present results (KBM)	
	C_f	*Sh*	C_f	*Sh*
0.22	3.1068	0.4515	3.1069	0.4511
0.60	2.4548	0.8431	2.4546	0.8429
0.78	2.2767	1.0214	2.2759	1.0216
0.94	2.1540	1.1745	2.1543	1.1748
2.0	2.9039	0.4010	2.9038	0.4011

4 Results and discussion

The current portion of the work highlights the physical perspective of BNF's flow past a semi-infinite vertical plate

with the (*Da-Fs*) model. The Keller-box finite difference technique is applied to solve the requisite posited equations. A detailed graphical illustration of the solution is shown in Figures 1–13 utilizing MATLAB code, on velocity (f'), temperature (θ), and nanoparticle volume fraction concentration (ϕ), skin friction coefficient (C_f), Nusselt number (Nu), Sherwood number (Sh) for the distinct dimensionless parameters. The numerical problem comprises two independent space variables (ξ, η), therefore, the non-similar results are obtained. The following default values like $Pr = 0.71$, $Sc = 0.6$, $Nr = 0.1$, $Nb = 0.3$, $Nt = 0.3$, $R = Da = Fs = 0.5$, $Gr = 10$, $\xi = 1.0$ are chosen for the simulation purposes.

Figure 1(c–e) depict the implications of thermal radiation (R), where ($0 \leq R \leq 1.1$) on velocity, temperature and concentration profiles. Mathematically, the radiative parameter is expressed as $R = \frac{16\sigma^* T^3_\infty}{3kk^*}$. From the expression, it is clear that the radiative parameter effectively alters the nanofluid's thermal conductivity, which significantly affects heat transmission. Thermal radiation ceases to exist at $R = 0$. Nevertheless, as R rises, thermal radiation becomes progressively more significant to the regime [56]. Although radiation only directly influences the temperature field while the coupling components in the momentum and nanoparticle concentration BLEs allow thermal radiation to have an indirect influence on these fields. Figure 1c shows that velocity increases due to increase values of the radiative parameter. Increasing R values correlate with the flow acceleration. Figure 1d illustrates that, as expected, a large increase in temperature occurs when the value of R increases. The regime is substantially electrified by radiative flux, resulting in a thicker thermal boundary layer. Furthermore, it reveals that greater R values result in improved heat transmission, which improves thermal profiles. Figure 1e demonstrates that the opposite effect is caused in nanoparticle concentration, with a decrease in concentrations accompanying higher values of R. When there is no radiative heat flux, nanoparticle concentration is clearly at its highest. Thinner species boundary layer thickness results in higher radiative effects. The physical relevance is that as thermal radiation increases, the velocity, temperature of the nanofluid increase because the radiative heat transfer raises the overall thermal energy in the regime. This additional heat energy reduces fluid viscosity, facilitating faster flow and stronger rotational motion. The increased temperature accelerates fluid motion, enhancing convective heat transfer. Simultaneously, the elevated thermal environment reduces the tendency for nanoparticles to cluster near the surface, leading to a decrease in nanoparticle concentration as they disperse more readily into the fluid.

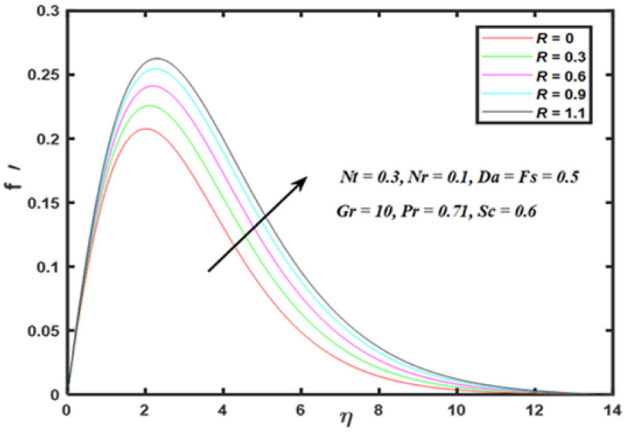

Figure 1c: Velocity profile for distinct values of *R*.

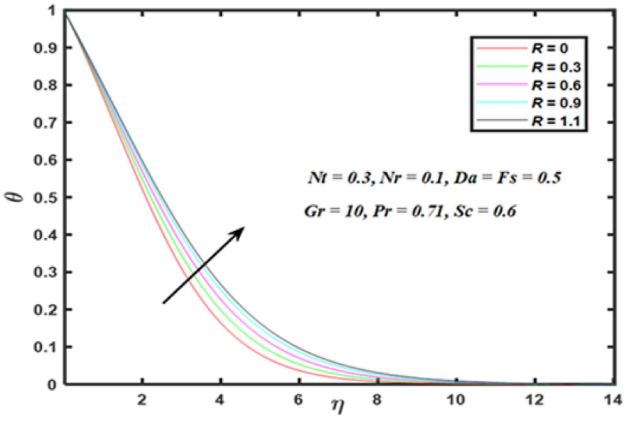

Figure 1d: Temperature profile for distinct values of *R*.

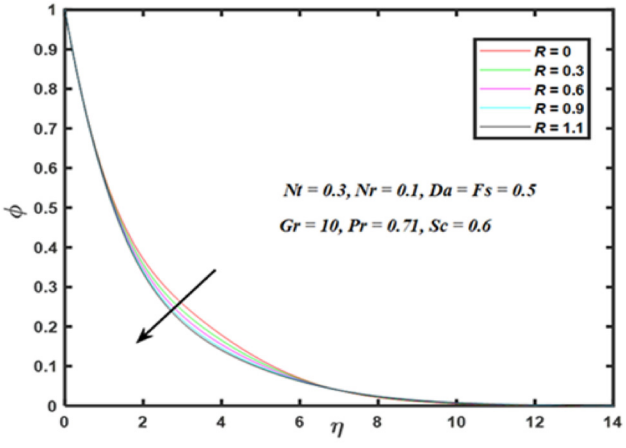

Figure 1e: Concentration profile for distinct values of *R*.

Figure 2(a–c) show the impact of Brownian motion ($0.3 \leq Nb \leq 1.5$) on velocity, temperature and concentration profiles. (Nb) defined as the ratio of the Brownian diffusion

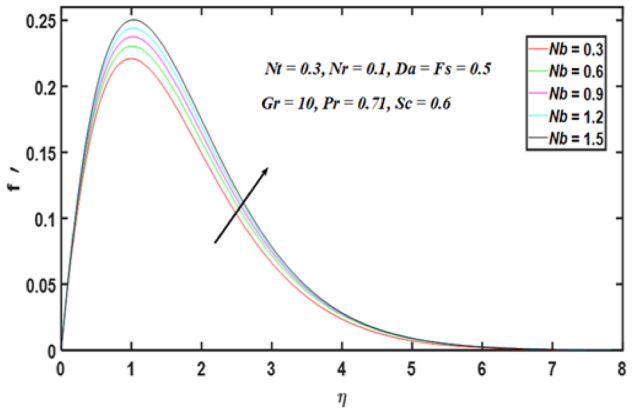

Figure 2a: Velocity profile for distinct values of *Nb*.

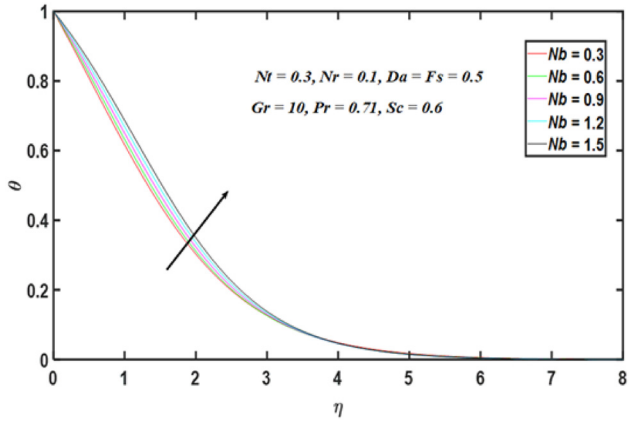

Figure 2b: Temperature profile for distinct values of *Nb*.

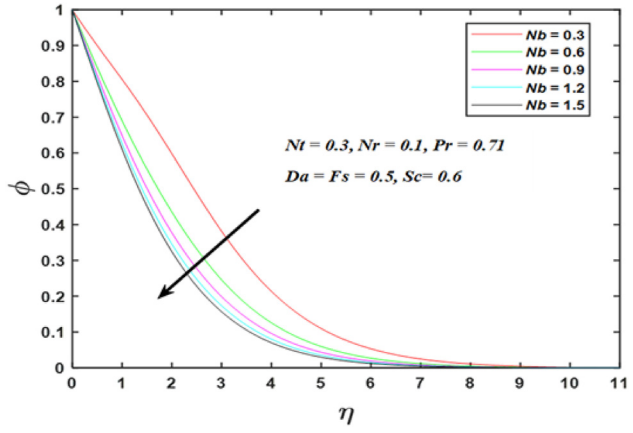

Figure 2c: Concentration profile for distinct values of *Nb*.

coefficient to the thermal diffusivity of the base fluid. This parameter is utilized to quantify the effects of Brownian motion on the heat and mass transmission characteristics of NFs. In Figure 2a Velocity profile is enhanced, although a stronger elevation is computed in the former with greater *Nb* values. Brownian motion also modifies the NF thermal conductivity and the propensity for heat transmission in the NF. As a result, the increased random motion of the NPs modifies the thermal pattern as well, and the momentum field experiences this influence through thermal buoyancy. As *Nb* increases, (θ) is positively affected across the BL regime, as seen in Figure 2b. There is also a significant change in the topology of (θ) profiles further from the substrate (wall) at very high *Nb* values. Raising the (θ) aggravates the motion of the NPs and ballistic collisions. Consequently, chaotic Brownian motion is increased even further. The increased heat conduction in the regime and the improved micro-convection surrounding the NPs are also influenced by the change in thermal conductivity with greater Brownian motion. This results in a thicker thermal BL due to a heating effect. Although the fluid's molecules and NPs are always moving, there is a noticeable overall shift in (θ). Brownian motion, however, predominates in the random thermal motion of the NPs. As *Nb* is increased, there is a notable decrease in (ϕ) values, as observed in Figure 2c. Hence, the thickness of the nanoparticle concentration boundary layer is reduced. Our findings are consistent with those of Reddy et al. [5] and Gaffar et al. [44], who have demonstrated that higher viscosity operates to boost heat convection and flow while decreasing mass transfer rates. The physical significance of these observations lies in the complex interplay between Brownian motion and NF dynamics. As *Nb* increases, NPs experience enhanced random movement, facilitating more efficient thermal diffusion and increasing fluid velocity. This phenomenon is crucial in settings where efficient heat transport is necessary, like cooling structures and thermal management in engineering. However, the reduction in concentration gradient signifies a more homogeneous dispersion of NPs, which can affect processes reliant on localized concentrations, such as drug delivery or materials synthesis. The fluid's Brownian motion is significantly impacted by increasing *Nb* levels because of the NPs' random mobility.

Figure 3(a–c) depict the influence of the thermophoresis parameter ($0 \leq Nt \leq 0.8$) on (f'), (θ), (ϕ) profiles. Driving NPs under a temperature gradient is known as thermophoresis. *Nt* quantifies the impact of thermophoretic force, which drives NPs from hot regions to cold regions, causing the fluid temperature to be modified within a fluid. The definition of the thermophoresis parameter is a ratio of the thermophoretic diffusion coefficient to the thermal diffusivity of the base fluid. From Figure 3a, an increase in *Nt* decelerates velocity (f'). The increasing thermophoresis parameter value enhances (θ) in Figure 3b and considerably boosts (ϕ) in Figure 3c. These trends are sustained at all distances transverse to the substrate. However, while

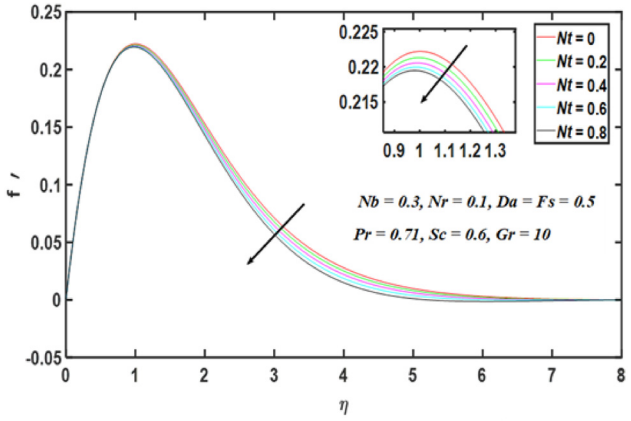

Figure 3a: Velocity profile for distinct values of *Nt*.

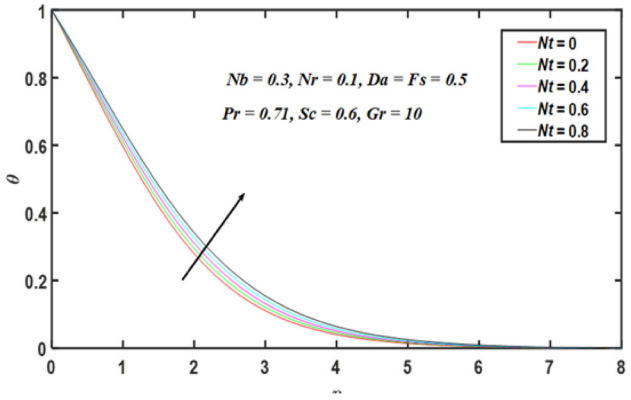

Figure 3b: Temperature profile for distinct values of *Nt*.

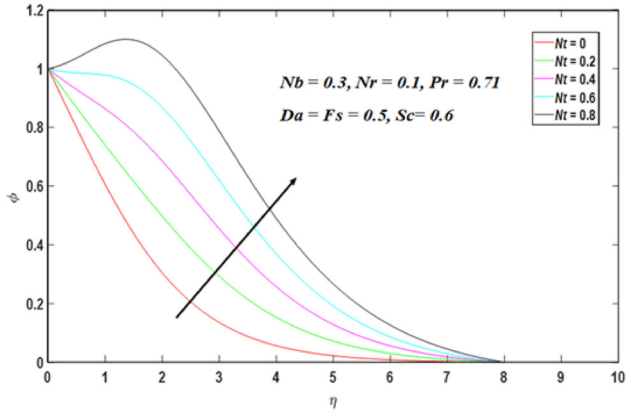

Figure 3c: Concentration profile for distinct values of *Nt*.

asymptotic decays occur from the wall to the free stream for all (θ) profiles, the nanoparticle concentration profile is only a decay for $Nt = 0$, which has not been identified previously in the literature. As *Nt* increases, the topology is flipped from a convex to a concave one for $Nt = 0.2$. With subsequent elevation in the thermophoresis parameter, a peak in nanoparticle concentration emerges progressively further from the wall. Eventually, however, profiles for $Nt > 0.2$ do descend smoothly to the free stream. Overall, stronger thermophoresis elevates the thermal and nanoparticle species BLT, which inevitably influences the structure of the coating regime. The impact of a higher thermophoretic temperature gradient is significant on all transport characteristics, confirming the important role it plays in NF mechanics. Our findings support the patterns of Reddy et al. [7, 42] and Gaffar et al. [44]. The Physical significance is that this signifies that a stronger thermophoretic force leads to enhanced momentum, heat, and mass transfer, reflecting more pronounced thermal and solute gradients in the NF flow.

Figure 4(a–c) elucidate the impact of the combined Buoyancy ratio parameter, ($-0.7 \leq Nr \leq 0.1$), on profiles (f'), (θ, (ϕ) through surface regime with transverse coordinate (η). Dual natural convection currents mobilized by temperature and nanoparticle species are present. The regime exhibits buoyancy from both thermal and nanoscale species, resulting in dual natural thermo-solute convection. If $Nr < 0$, the forces of thermal buoyancy and species buoyancy forces are opposed to each other. If $Nr = 0$, forced convection occurs, and buoyancy forces disappear. For $Nr > 0$, the buoyancy force helps the other. As seen in Figure 4a, Velocity (f') is suppressed with positive *Nr* but is enhanced with negative *Nr*. In other words, assistive buoyancy damps the primary flow, whereas opposing buoyancy enhances it. This reduction weakens buoyancy-driven movement, tending to a decrease in fluid velocity. Consequently, with less buoyancy force driving fluid motion, the convective heat transfer process is hindered, resulting in depreciation of velocity profiles in the system.Figure 4(b and c) demonstrates that an increment of *Nr* strengthens the buoyancy-driven flows. This augmentation enhances fluid motion, facilitating more effective mixing and transport of heat and solute. Consequently, (θ) and (ϕ) profile appreciates.

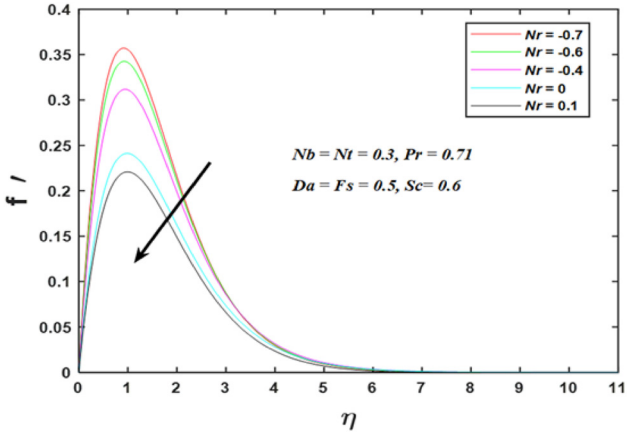

Figure 4a: Velocity profile for distinct values of *Nr*.

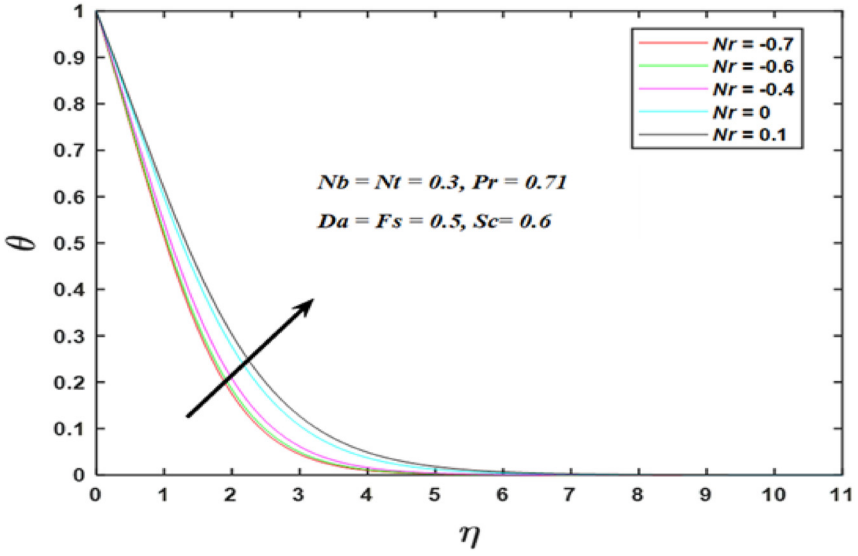

Figure 4b: Temperature profile for distinct values of *Nr*.

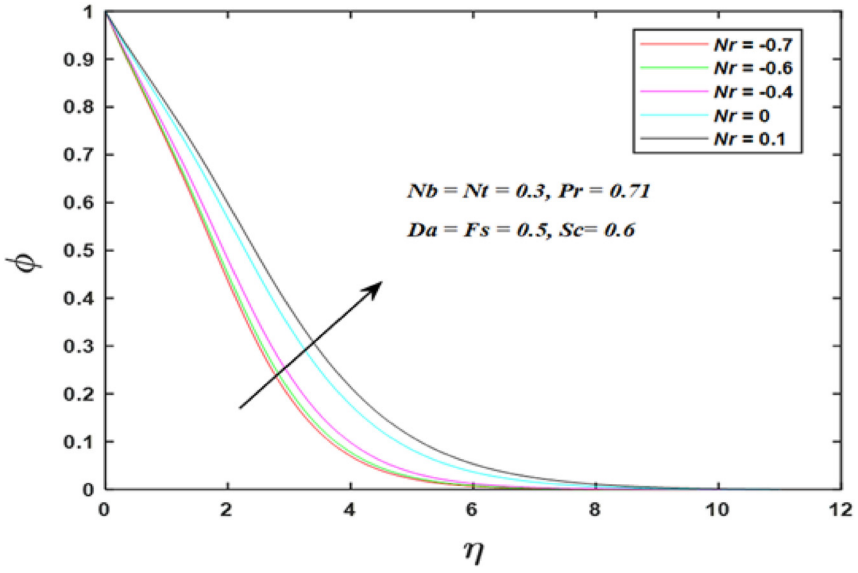

Figure 4c: Concentration profile for distinct values of *Nr*.

Notably, both (θ) and (ϕ) profiles show an upward trend, signifying that the heightened internal buoyancy forces improve heat, mass transfer. This results in higher thermal, solute gradients near the surface, causing increased (θ), (ϕ) levels within the boundary. Our outcomes align with the observed trends of Reddy et al. [7, 42] *and* Gaffar et al. [44]. Physically, this signifies that stronger buoyancy effects lead to more efficient energy and species transport in the fluid. This is essential for precisely estimating flow behaviour and maximising mass and heat transfer in a variety of technical applications.

Figure 5(a–c) portray the impact of Darcy number (*Da*), where ($0.2 \leq Da \leq 1.8$), on profiles (f'), (θ), (ϕ). Particularly in the study of flow via porous media, *Da* is a dimensionless number that characterizes the relative permeability of the medium. *Da* is used to compare the effects of inertial forces and the resistance of the porous material to the movement of fluid. A high *Da* implies that inertial forces are more essential, whereas a low *Da* denotes that the flow is mostly controlled by the resistance of the porous medium. Figure 5a demonstrates that (f') is amplified with a hike in *Da*, with the maximum effect occurring close to the surface. Greater permeability indicates a decrease in solid Fibers that obstruct axial flow; this lowers the Darcian resistance and accelerates the flow. Elevating pushes peak velocity even more *Da*. Figure 5b shows that boosting the

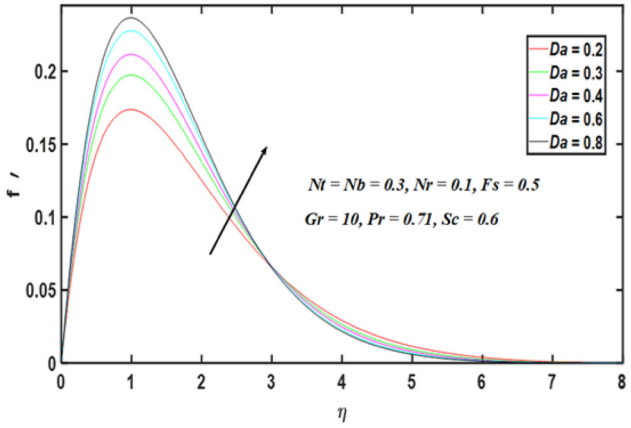

Figure 5a: Velocity profile for distinct values of *Da*.

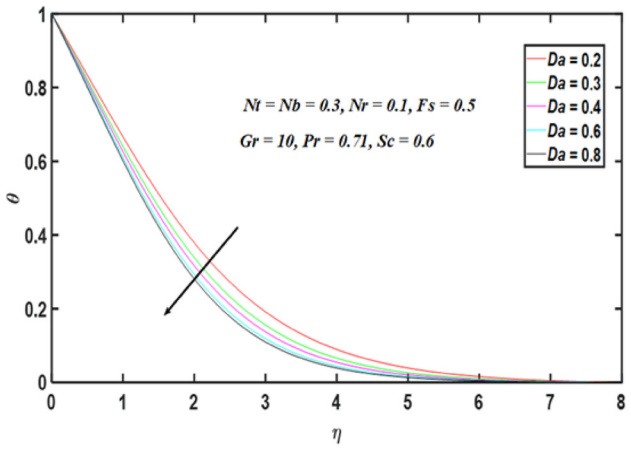

Figure 5b: Temperature profile for distinct values of *Da*.

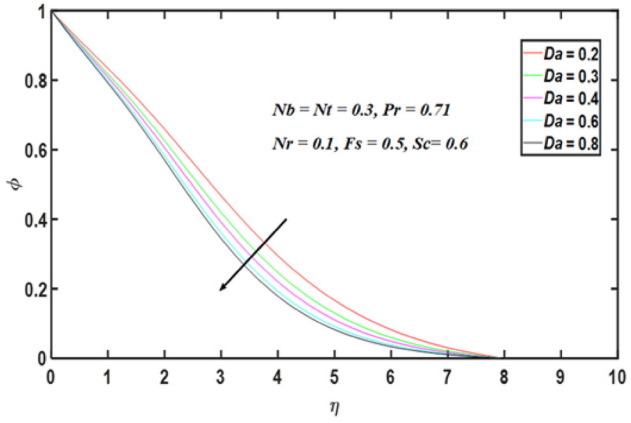

Figure 5c: Concentration profile for distinct values of *Da*.

Darcy parameter yields a significant suppression of (θ). Heat conduction is suppressed as a result of the loss of solid fibers in the porous matrix linked to increased penetration. This cools the regime by reducing heat diffusion inside it. As a result, the surface's heat BLT is suppressed. Porous media

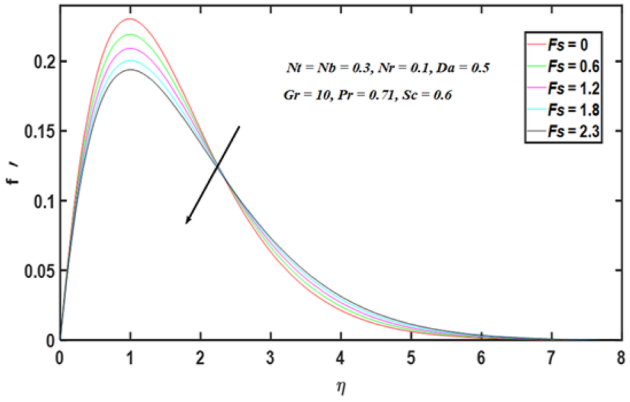

Figure 6a: Velocity profile for distinct values of *Fs*.

with lower permeability reach far higher temperatures than those with higher permeability. Figure 5c eluciates that as the *Da* increases, this indicates increased resistance to pass through the porous substance. This resistance reduces the exchange of nanocrystals and leads to a low concentration of NPs in the vicinity. Consequently, the overall (ϕ) profile within the fluid decreases. Our outcomes are consistent with the patterns of [7, 17, 44]. Physically, fluid flow resistance falls as *Da* rises, showing increased permeability in the porous media. This lower resistance allows for an increased fluid velocity because the flow encounters less drag. However, the enhanced fluid velocity reduces leads to decay in both (θ) and (ϕ) profiles. Essentially, fluid moves more quickly through the medium, carrying less heat and fewer NPs along with it. Reduced heat transmission via thermal conduction in the system is facilitated by the steady reduction of solid fibres that have large *Da* values in a porous medium. This cools down the thermal BLT, which also diminishes and limits the transfer of thermal energy from the vertical surface into the system. Consequently, the presence of porous materials significantly affects the system's speed and thermal dispersion, offering a solid foundation for regulating flow and temperature management. This parameter is crucial for analysing and modelling fluid flow patterns in applications involving porous media, such as filtration, groundwater flow, and enhanced oil recovery.

Figure 6(a–c) Influence of the Forchheimer number ($0 \leq Fs \leq 2.3$) on (f'), (θ), (ϕ) profiles across the farthest domain with transverse coordinates (η) is discussed. The dimensionless parameter (*Fs*) is used to describe how inertial forces affect porous media flow. It measures relative significance of viscous forces and inertial effects in a medium with pores. A greater *Fs* means that inertial implications, which affect the flow properties through the porous media, become of greater significance in comparison to viscosity forces. Figure 6a demonstrates how a greater inertial

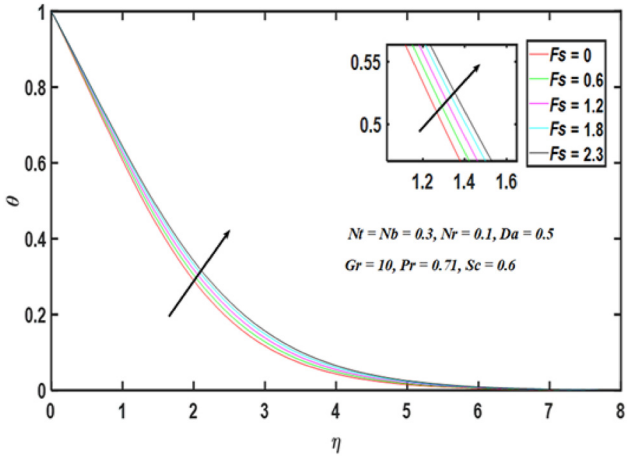

Figure 6b: Temperature profile for distinct values of *Fs*.

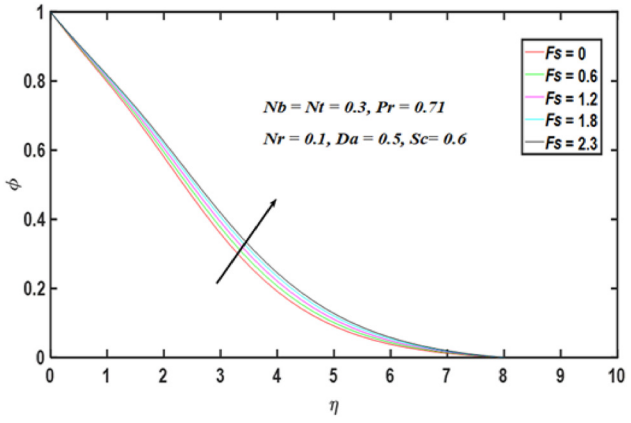

Figure 6c: Concentration profile for distinct values of *Fs*.

impedance that resists flow is present and causes a noticeable depreciation in velocity with an increase in (*Fs*). This impact is maximized close to the surface; a lesser deceleration in a flow with a higher (*Fs*) is calculated farther away. There is no discernible effect of (*Fs*) on flow in the free stream. Figure 6b reveals that a significant heating impact occurs in the regime as a result of the higher *Fs*. Temperature (θ) is always stronger for all transverse coordinate (η) values. Hence, the thickness of thermal BL is highest for the strong Forchheimer case ($Fs = 1$) and the smallest for the weak Forchheimer drag case ($Fs = 0$). Figure 6c illustrates that (ϕ) increases as (*Fs*) gradually rises because greater (*Fs*) signifies greater inertial effects in flow through a porous medium. These inertial effects enhance the mixing and dispersion of nanocrystals, leading to a greater (ϕ) of NPs near surface. Consequently, increased inertial forces facilitate better nanoparticle distribution and an elevated (ϕ) profile. Our outcomes are consistent with the patterns of [7, 16, 44]. Physical interpretation is that since the drag force and coefficient of inertia are connected, a surge in inertia causes the fluid's drag force to grow, thus lowering its speed. The influence of the quadratic inertial drag is larger with closer proximity to the wall's surface. Thus, velocity (f') dampens while temperature (θ) and concentration (ϕ) profiles enhance with higher *Fs* numbers. (*Fs*) is used to optimize flow and performance in NF-based filtration systems and heat exchangers by accounting for inertial effects in porous media.

Figure 7(a–c) indicate the impact of Prandtl number (*Pr*), where ($0.3 \leq Pr \leq 1$) on profiles (f'), (θ), (ϕ). *Pr* is a non-dimensional number; it characterizes momentum diffusion's (viscous effects) relative significance to thermal diffusion (heat conduction) in a fluid. Its literal meaning is the kinematic viscosity to thermal diffusivity ratio. Figure 7(a–c) demonstrate that when the Prandtl number *Pr* increases, the velocity (f') profile appreciates, but temperature (θ) profiles decrease because a higher *Pr* implies that viscous forces dominate over thermal diffusion, slowing the flow and reducing heat transfer efficiency. A higher *Pr*

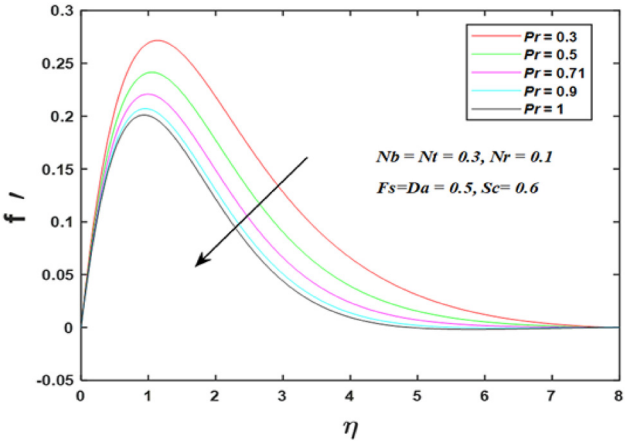

Figure 7a: Velocity profile for distinct values of *Pr*.

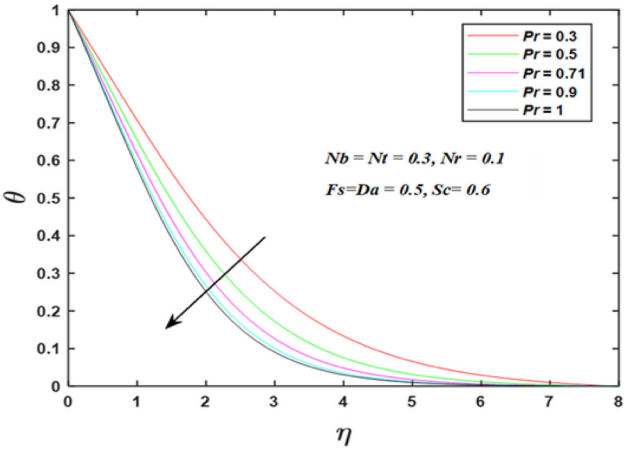

Figure 7b: Temperature profile for distinct values of *Pr*.

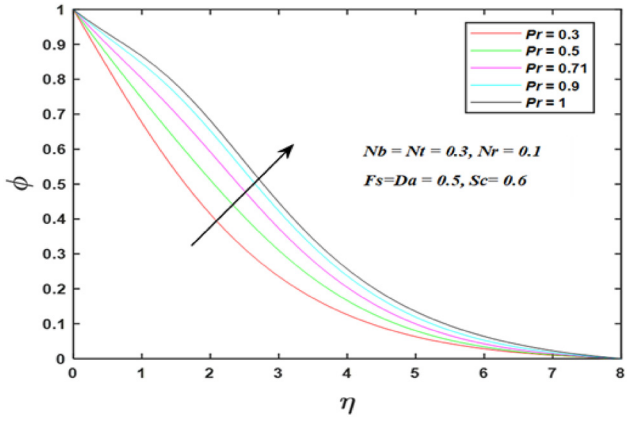

Figure 7c: Concentration profile for distinct values of *Pr*.

means less thermal diffusion, which leads to slower heat transfer within the BL. Conversely, the nanoparticle (ϕ) increases because the reduction in thermal diffusion limits the influence of thermal gradients, allowing more NPs to accumulate near the surface. The Physical significance is that this indicates that in high-Prandtl-number fluids, heat conduction is less efficient, while (ϕ) remains more stable, emphasizing the dominance of viscous and concentration effects over thermal effects in such flows. Realistic application of *Pr* involved improving the thermal efficiency of heating, ventilation, and air conditioning (HVAC) systems by using NFs with suitable Prandtl numbers for better heat transfer rates. In the unimpeded stream, every profile is shown to converge seamlessly.

Figure 8(a–c) Features impact of Schmidt number (*Sc*), where ($0.71 \leq Sc \leq 5$) on profiles (f'), (θ), (ϕ) through surface regime with transverse coordinate (η). Schmidt number (*Sc*) dimensionless number that characterizes the relative significance of mass diffusion (molecular diffusion) over

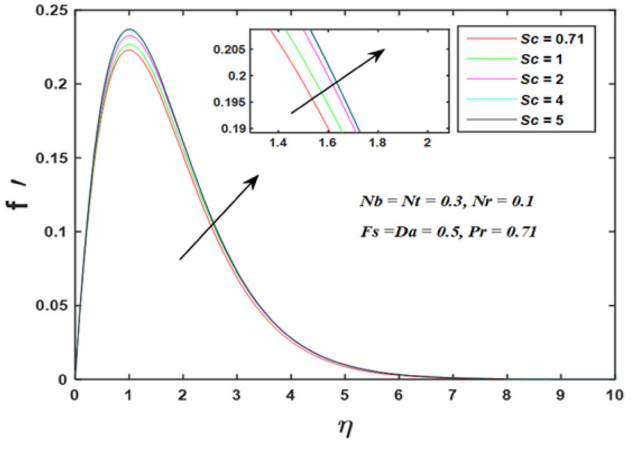

Figure 8a: Velocity profile for distinct values of *Sc*.

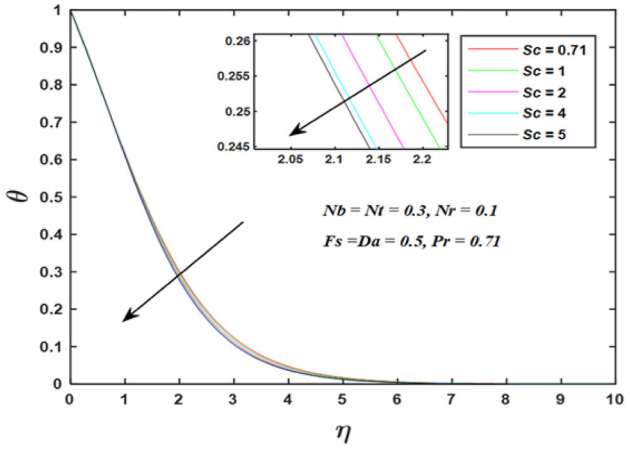

Figure 8b: Temperature profile for distinct values of *Sc*.

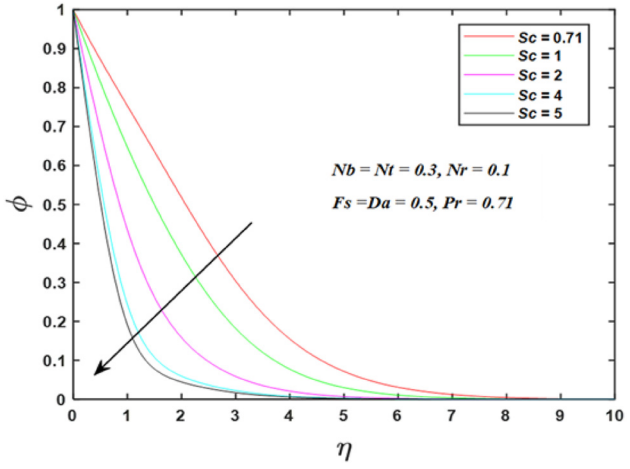

Figure 8c: Concentration profile for distinct values of *Sc*.

momentum diffusion (viscous effects) in a fluid. Figure 8(a–c) elucidates that as Schmidt number *Sc* increases velocity profile rises because a higher *Sc* implies that mass diffusivity is much lower than momentum diffusivity, resulting in less resistance to momentum transfer, thus enhancing fluid flow. Meanwhile, the temperature (θ) and concentration (ϕ) decrease because higher *Sc* values reduce mass diffusivity, limiting both heat and nanoparticle diffusion away from the surface. This leads to a thinner BL for (θ) and (ϕ) profiles. The Physical viewpoint is a higher *Sc* indicates that mass diffusion is restricted, allowing for faster fluid flow (higher velocity) but reduced efficiency in both heat transfer and nanoparticle dispersion, which affects the overall convection and transport processes in the fluid. The physical application of *Sc* is to optimize mass transfer processes in applications such as chemical reactors and separation technologies by selecting NFs with appropriate momentum and mass diffusion properties.

Figure 9(a–c) demonstrate the impact of Grashof number ($0.71 \leq Gr \leq 10$) on profiles (f'), (θ), (ϕ) through surface regime with transverse coordinate (η). (Gr) a non-dimensional number which quantifies the proportionate importance of buoyant and viscous forces in a fluid flow. It helps in understanding and optimizing heat transfer processes driven by buoyancy effects. Figure 9(a–c) As Gr increases, (f') increases due to stronger buoyancy forces driving the flow, enhancing fluid motion. Temperature (θ) and Concentration (ϕ) profiles decrease because the intensified convection transfers heat and NPs more rapidly away from the surface, thinning the BLs. The physical significance is that a higher Gr indicates dominant buoyancy effects, leading to faster fluid flow and more efficient heat and mass transfer, but reduced BLT for (θ), (ϕ) fields. It helps predict how buoyancy-driven flow affects heat and mass transfer, allowing for improved efficiency in these thermal management systems.

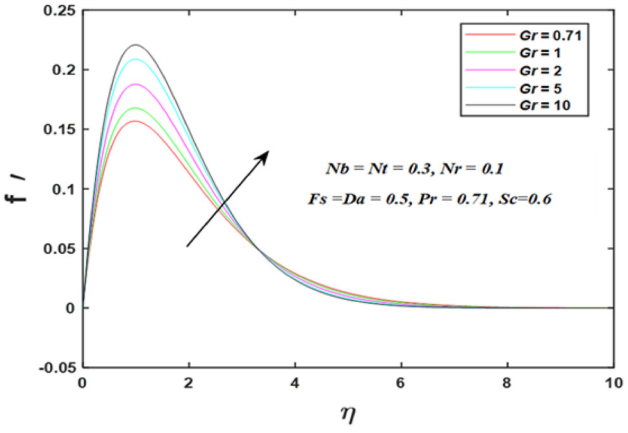

Figure 9a: Velocity profile for distinct values of Gr.

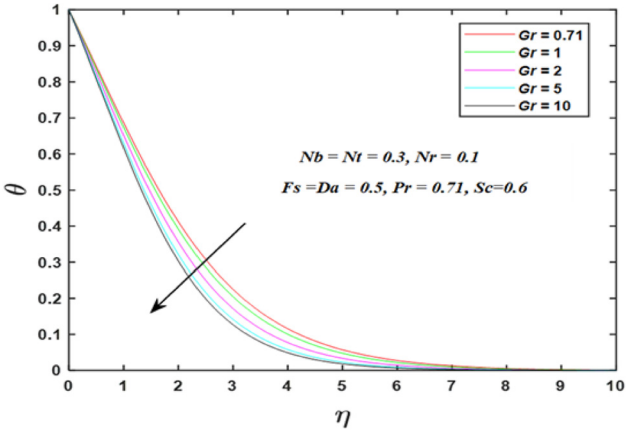

Figure 9b: Temperature profile for distinct values of Gr.

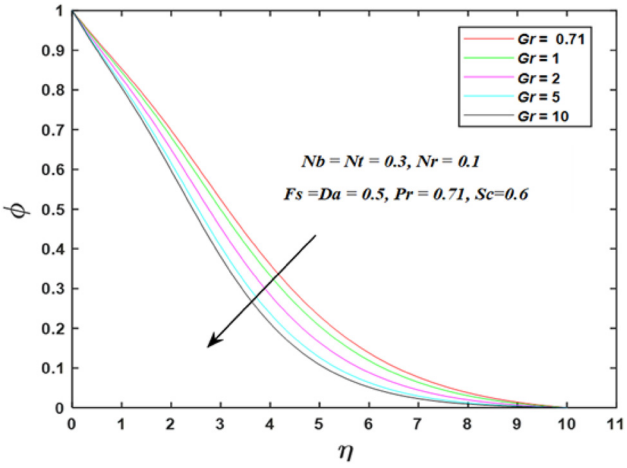

Figure 9c: Concentration profile for distinct values of Gr.

Notably, the preceding graphs show that all profiles in the free stream converge smoothly, indicating the use of an appropriate large infinity boundary condition.

Figures 10(a–c) illustrate the impacts of the Darcy parameter (Da) on higher magnitudes of skin friction (C_f), Sherwood number (Sh), and Nusselt number (Nu), are computed with an increase in streamwise coordinate ($0 \leq \xi \leq 3$). A substantial boost of Da decreases flow resistance within the porous medium, leading to higher fluid velocities. This reduction in resistance enhances shear stress at the surface, increasing C_f, momentum BLT is enhanced. Additionally, with improved flow velocities, convective mass and heat transfer are more efficient, resulting in higher Sh, Nu. The higher velocity promotes better mixing and dispersion of NPs, which improves Nu, Sh near the surface produces significant heating, and nanoparticle volume, and escalates thermal concentration BLT. Physical relevance is, higher Da enables more effective convective transport, leading

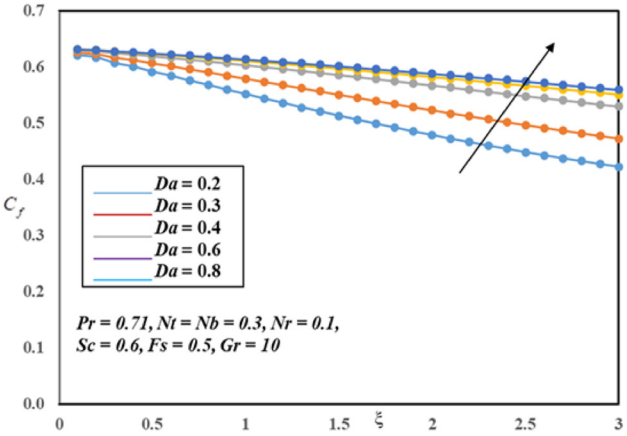

Figure 10a: Variation in skin friction for distinct values of Da.

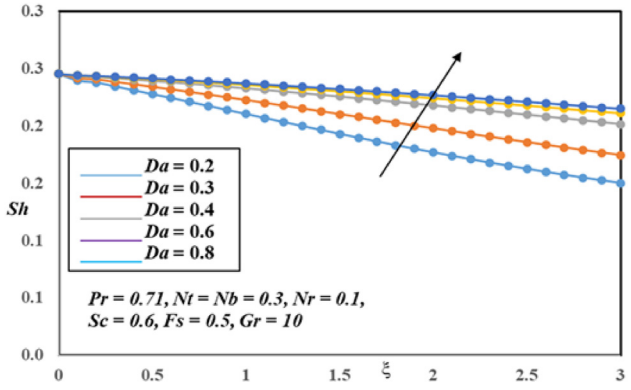

Figure 10b: Variation in Sherwood number for distinct values of *Da*.

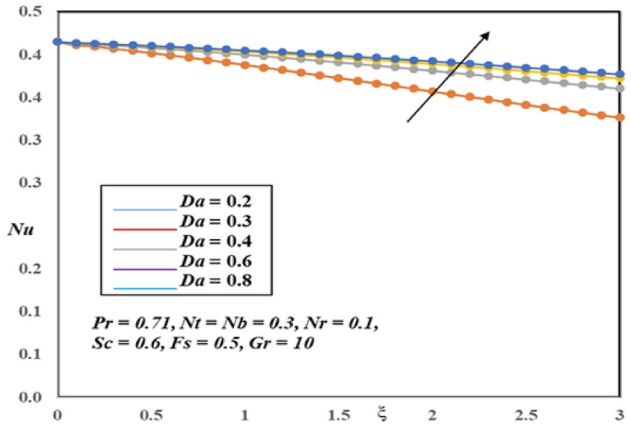

Figure 10c: Variation in Nusselt number for distinct values of *Da*.

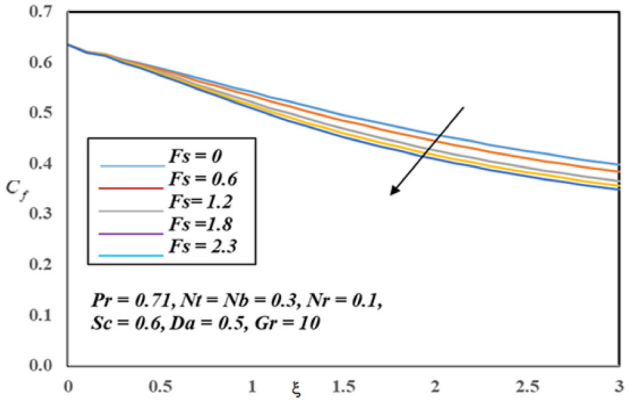

Figure 11a: Variation in skin friction for distinct values of *Fs*.

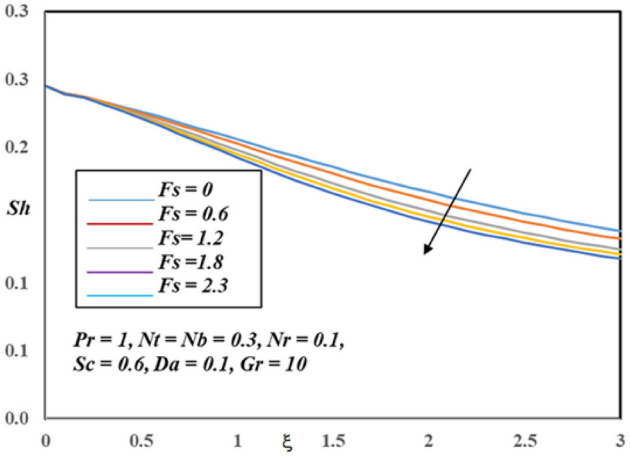

Figure 11b: Variation in Sherwood number for distinct values of *Fs*.

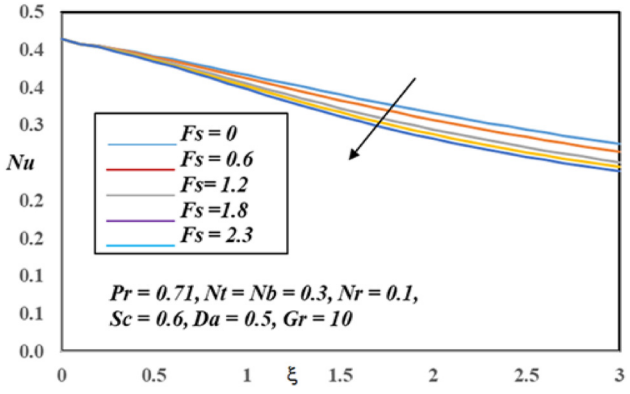

Figure 11c: Variation in Nusselt number for distinct values of *Fs*.

to improved thermal and mass transfer performance. In real-life applications, increasing the *Da* enhances the efficiency of mass and heat transmission in systems such as advanced cooling systems, chemical reactors, and filtration units. Improved (C_f), *Sh* and *Nu* indicate better performance in heat dissipation and particle transport, optimizing processes like electronic cooling and water treatment."

Figure 11(a–c) demonstrate the impacts of (*Fs*), on (C_f, *Sh*, *Nu*), along surface regime at higher streamwise coordinate values ($0 \leq \xi \leq 3$). A substantial rise in *Fs* signifies a rise in inertial effects relative to viscous forces in the porous medium. This shift causes increased flow resistance and turbulence, leading to reduced fluid velocities. Consequently, C_f decreases due to less effective shear stress at the surface. Additionally, enhanced inertial effects disrupt the BLs, reducing the efficiency of both mass and heat transmission. As a result, *Nu*, *Sh* declined due to decreased convective effectiveness, reflecting poorer thermal and particle transport performance. Moreover, this elucidates that appreciation of *Fs* values causes a remarkable decline in the heat and mass transport to the substrate. Thermal and concentration BLT is condensed and has a large heating influence because of a net heat, mass transfer into BL.

Figure 12(a–e) illustrates how engineering interest quantities (C_f, *Sh*, *Nu*) respond to a variety of associated components. In Figure 12a. Substantial increase (C_f) is noted with an improvement in the Forchheimer number (*Fs*) and

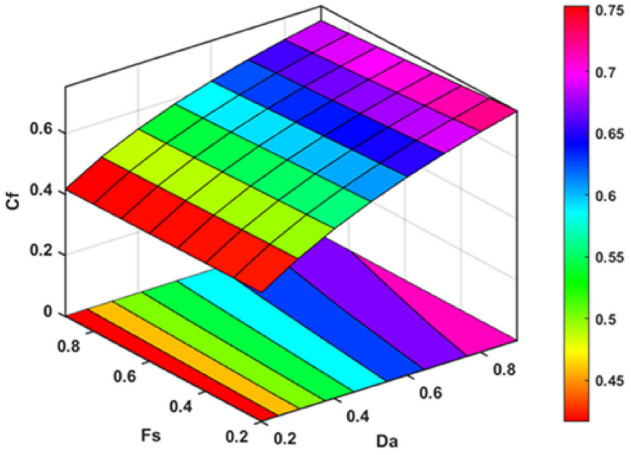

Figure 12a: Surface contour plot variation for distinct values of *Da*, *Fs* against C_f.

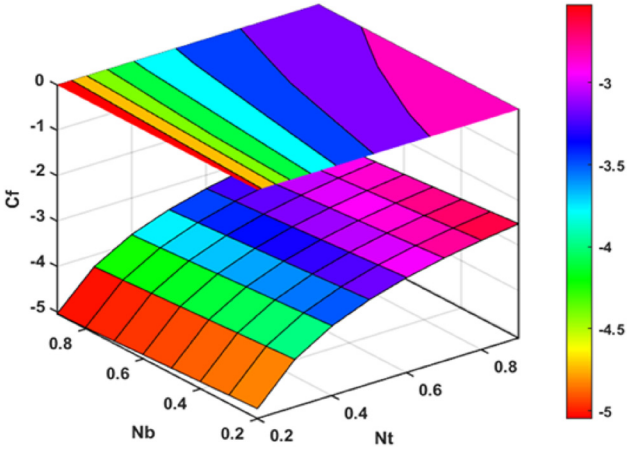

Figure 12b: Surface contour plot variation for distinct values of *Nb*, *Nt* against C_f.

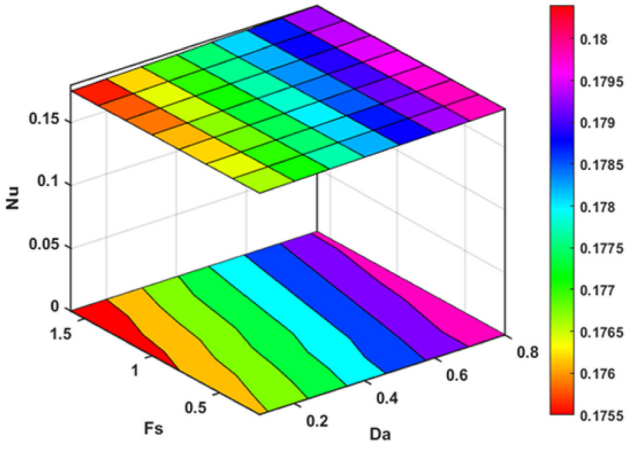

Figure 12c: Surface contour plot variation for distinct values of *Da*, *Fs* against *Nu*.

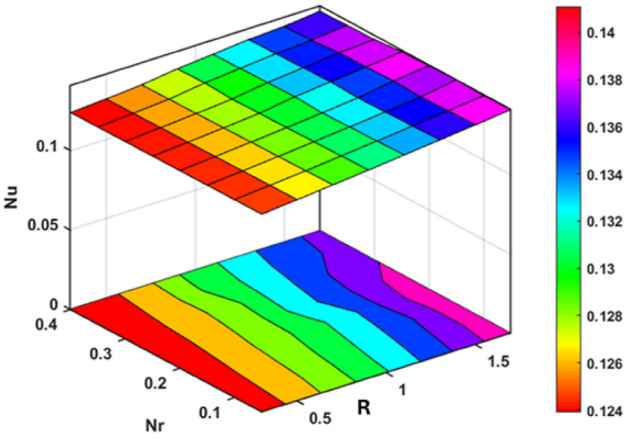

Figure 12d: Surface contour plot variation for distinct values of *Nr*, *R* against *Nu*.

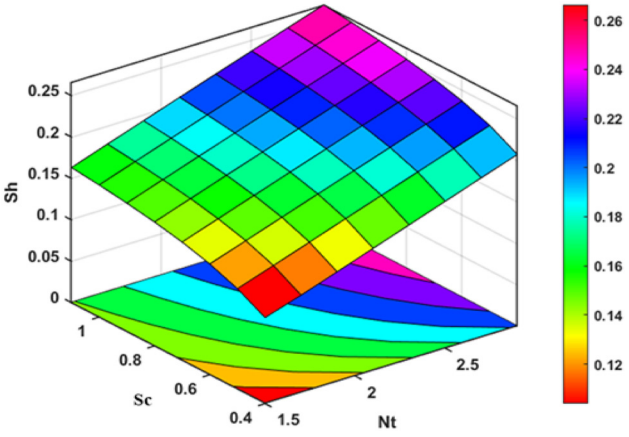

Figure 12e: Surface contour plot variation for distinct values of *Sc*, *Nt* against *Sh*.

Darcy number (*Da*) and readings. A surface plot of C_f for different values of (*Nb*) and (*Nt*) is shown in Figure 12b. It portrays that skin friction appreciates significantly as (*Nb*) and (*Nt*) parameters expand. The surface plot in Figure 12c shows that *Nu* improves as the Forchheimer number (*Fs*) and Darcy number (*Da*) grow. Moreover, in Figure 12d, the Nusselt number *Nu* improves as the Buoyancy number (*Nr*) and Thermal radiation (*R*) elevate. The implication of (*Sc*) and thermophoresis (*Nt*) on *Sh* is illustrated in Figure 12e. The mass profile thickening and the (*Sc*) pattern are further amplified as the value of (*Nt*) grows, which also contributes to the enhancement of the dimensionless Sherwood number *Sh* (Figure 13(a and b)).

Table 4 shows (C_f, *sh*, *Nu*) for various values of *R*, *Pr*, *Sc*, *Da*, *and Fs* along with a variation in the stream-wise coordinate value ξ, ($1 \leq \xi \leq 3$). Here $Nr = 0.1$, $Nb = 0.3$,

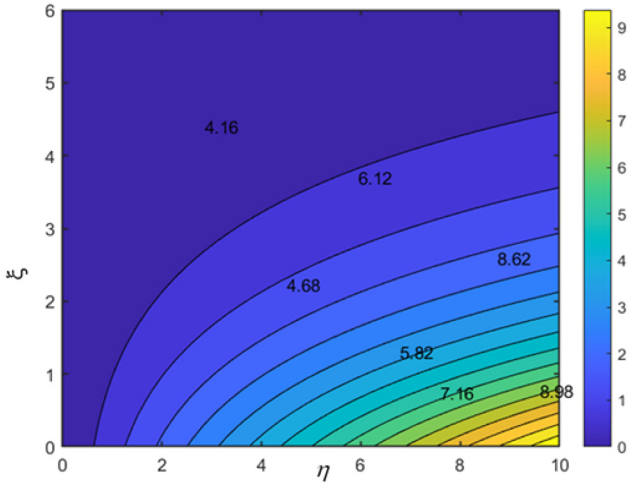

Figure 13a: Isotherms for different Darcy values when $Pr = 0.71$.

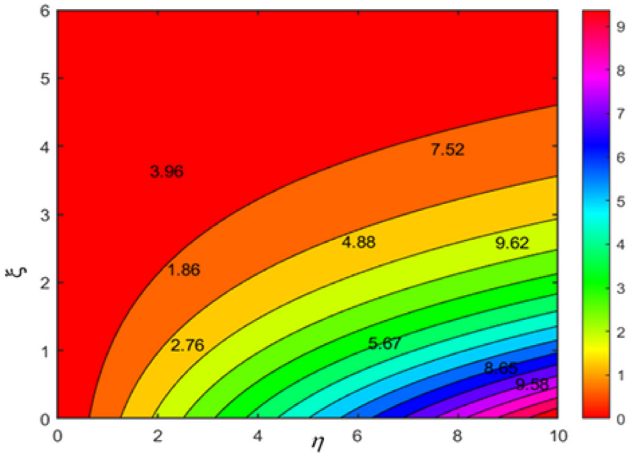

Figure 13b: Isotherms for different Forchheimer values when $Pr = 0.71$.

$Nt = 0.3, Ec = 0.5, Gr = 10$. It *is noted that as radiation parameter* (R) *appreciates* (C_f), (Sh) damps conversely (Nu) hikes. Moreover, the *Prandtl number Pr appreciates* the fluid's thermal diffusivity decreases, leading to a thicker thermal BL, reducing (Nu). Elevation in Pr also means higher momentum diffusivity, which depreciates (C_f). Conversely, mass diffusivity is less affected, resulting in a thinner concentration BL and an increased Sh, indicating enhanced mass transfer. As (Sc) boosts, it leads to a thinner concentration BL. This results in higher mass transfer rates, thus steadily rising (Sh). The reduced mass diffusivity also means higher momentum diffusivity, which increases velocity gradient at the wall, thereby raising (C_f). Furthermore, the

Table 4: Values of skin friction (C_f), Sherwood number (Sh), and Nusselt number (Nu) for various values of R, Pr, Sc, Da, *and* Fs.

R	Pr	Sc	Da	Fs	$\xi = 1$			$\xi = 2$			$\xi = 3$		
					C_f	Sh	Nu	C_f	Sh	Nu	C_f	Sh	Nu
0					0.6538	0.4595	0.1663	0.7044	0.6913	−0.2435	0.7789	1.0699	−0.9435
0.3					0.6058	0.4421	0.1338	0.6253	0.6757	−0.3335	0.6888	1.0968	−1.2020
0.6					0.5576	0.4255	0.0969	0.5551	0.6725	−0.4377	0.6138	1.1604	−1.5138
0.9					0.5240	0.4152	0.0680	0.5107	0.6787	−0.5212	0.5688	1.2293	−1.7776
1.1					0.4953	0.4077	0.0404	0.4752	0.6900	−0.6021	0.5342	1.3086	−2.0478
	0.71				0.8859	0.6184	0.3013	1.0847	0.6015	0.2465	0.2249	0.5615	0.1211
	7				0.8436	0.6178	0.3200	1.0331	0.6030	0.2615	0.2062	0.5645	0.1265
	10				0.7667	0.6266	0.3365	0.9404	0.6151	0.2737	0.1753	0.5750	0.1283
	15				0.7306	0.6417	0.3257	0.8976	0.6305	0.2633	0.1622	0.5848	0.1206
	25				0.6980	0.6750	0.2830	0.8599	0.6614	0.2257	0.1510	0.6012	0.0988
		0.5			0.4953	0.4077	0.0404	0.4752	0.6900	−0.6021	0.5342	1.3086	−2.0478
		5			0.6389	1.2280	0.1047	0.6542	1.3713	−0.3097	0.7092	1.6445	−1.0732
		10			0.6413	1.5821	0.1034	0.6549	1.7005	−0.2934	0.7075	1.9364	−1.0249
		15			0.6422	1.8255	0.1040	0.6550	1.9312	−0.2827	0.7067	2.1495	−0.9963
		20			0.6426	2.0178	0.1049	0.6551	2.1154	−0.2750	0.7064	2.3232	−0.9764
			0.4		0.5144	0.1465	0.3971	0.4429	0.1196	0.3489	0.3900	0.1043	0.3090
			0.8		0.5536	0.1631	0.4206	0.5040	0.1431	0.3900	0.4591	0.1267	0.3596
			1.6		0.5730	0.1713	0.4317	0.5399	0.1634	0.4120	0.5109	0.3906	0.3835
			2.1		0.5822	0.1751	0.4368	0.5587	0.1800	0.4227	0.5344	0.1290	0.4077
			2.5		0.5846	0.1761	0.4381	0.5658	0.2317	0.4252	0.5421	0.1832	0.4111
				0.6	0.5268	0.1519	0.4046	0.4592	0.1258	0.3600	0.4067	0.1090	0.3213
				1.2	0.5136	0.1473	0.3958	0.4339	0.1179	0.3406	0.3773	0.1027	0.2967
				1.7	0.5037	0.1438	0.3891	0.4176	0.1133	0.3277	0.3600	0.1000	0.2821
				2.2	0.4947	0.1406	0.3829	0.4043	0.1099	0.3170	0.3465	0.0985	0.2705
				2.7	0.4865	0.1377	0.3771	0.3931	0.1072	0.3078	0.3355	0.0975	0.2611

enhanced flow mixing due to higher (*Sc*) contributes to surge heat transfer, resulting in a higher (*Nu*). As (*Da*) appreciates, the permeability of porous medium hikes, reducing resistance to fluid flow. This leads to higher fluid velocities near the wall, which elevates (C_f). The enhanced fluid motion improves both heat and mass transmission, resulting in higher (*Nu*), (*Sh*) due to thinner thermal and concentration BL. As (*Fs*) rises significantly, the inertial resistance in porous media becomes more significant. This increased resistance reduces (f'), leading to a decrease in (C_f). Additionally, the lower (f') diminishes both heat and mass transmission, resulting in reduced (*Nu*), (*Sh*) due to thicker thermal and concentration BL.

5 Main findings

In this study, we conducted numerical simulations to investigate the steady state laminar, incompressible, thermal radiative flow past a semi-infinite vertical surface embedded with Darcy–Forchheimer porous medium. Additionally, we considered the influence of the two-phase nanofluid model along with thermal convection, nanoparticle heat, and mass transfer in this context. After utilizing the pertinent variables, the required obtained equations are additional exercised by the well-known Keller-box scheme. The non-similar solutions are obtained in the form of graphs and tables for the several distinct controlling parameters. Consequences divulge the subsequent practical implications for enhancing the design and optimization of cooling systems, electronic thermal management, and energy systems in circumstances where accurate control of temperatures and effective heat transmission are essential. The significant findings from our study can be summarized as follows.

- The velocity and temperature profiles increased with rising values of the Brownian motion parameter while the concentration profile decreased.
- With increasing values of the thermophoresis parameter, the velocity profile shrinkages whereas the concentration and temperature profiles boosted up.
- The temperature distribution and concentration profiles raised due to the larger impacts of the buoyancy ratio parameter but the velocity profile shrank.
- The heat transfer rate upsurges due to the superior impacts of the radiation parameter while the mass transfer rate and shear stress abruptly decline.
- Owing to the rising values of the Darcy number, the gradients (shear stress, heat and mass transfer rates) escalated.
- The shear stress, heat and mass transfer rates decayed owing to the larger influences of the Forchheimer parameter.

6 Future work

Future research studies can be extended by incorporating non-Newtonian fluid characteristics, variable thermophysical properties, and time-dependent boundary conditions to interpret better the real-world scenarios. Future work may also involve coupling the numerical results with experimental validation to enhance reliability. Moreover, exploring three-dimensional and transient flow configurations, along with optimization through machine learning algorithms, could further enrich the understanding of nanofluid transport in advanced thermal systems.

Acknowledgments: The authors extend their appreciation to the Deanship of Scientific Research at Northern Border University, Arar, KSA, for funding this research work through the project number “NBU-FFR-2025-2225-17”.
Funding information: This research was funded by the Deanship of Scientific Research at Northern Border University, Arar, KSA, through the project number “NBU-FFR-2025-2225-17”.
Author contribution: All authors have accepted responsibility for the entire content of this manuscript and approved its submission.
Conflict of interest: The authors state no conflict of interest.
Data availability statement: All data generated or analysed during this study are included in this published article.

References

1. Choi SUS. Enhancing thermal conductivity of fluids with nanoparticles. In: Siginer DA, Wang HP, editors. Developments and Applications of Non-Newtonian Flows. New York, NY: ASME; 1995, vol 231:99—105 pp.
2. Raees A, Farooq U, Hussain M, Khan WA, Bashir Farooq F. Non-similar mixed convection analysis for magnetic flow of second-grade nanofluid over a vertically stretching sheet. Commun Theor Phys 2021;73:065801.
3. Kuznetsov AV, Nield DA. Natural convective boundary-layer flow of a nanofluid past a vertical plate. Int J Therm Sci 2010;49:243—7.
4. Buongiorno J. Convective transport in nanofluids. ASME J Heat Transfer 2006;128:240—50.
5. Ramesh Reddy P, Abdul Gaffar S, Beg OA, Hidayathulla Khan BM. Hall and ion-slip effects on nanofluid transport from a vertical surface: Buongiorno’s model. ZAMM-J Appl Math Mech 2022;102:e202000174.

6. Razzaq R, Farooq U, Cui J, Muhammad T. Non-similar solution for magnetized flow of Maxwell nanofluid over an exponentially stretching surface. Math Probl Eng 2021;10:1—10.
7. Cui J, Munir S, Farooq U, Rabie MEA, Muhammad T, Razzaq R. On numerical thermal transport analysis of three dimensional bioconvective nanofluid flow. J. Mathematics 2021;2021:11.
8. Halwe-Pandharikar A, Deshmukh SJ, Jee Kanu N. Numerical investigation and experimental analysis of nanoparticles modified unique waste cooking oil biodiesel fueled CI engine using single zone thermodynamic model for sustainable development. AIP Adv 2022;12:095218.
9. Pandey V, Kanu NJ, Singh GK, Gadissa B. AZ31-alloy, H13-die combination heat transfer characteristics by using inverse heat conduction algorithm. Mater Today Proc 2021;4:4762—6.
10. Zhou G, Huang J, Li H, Li Y, Jia G, Song N, et al. Multispectral camouflage and radiative cooling using dynamically tunable metasurface. Opt Express 2024;32:12926—40.
11. He J, Hou Q, Yang X, Duan H, Lin L. Isolated slug traveling in a voided line and impacting at an end orifice. Phys Fluids 2024;36:027105.
12. Deng Z, Umbanhowar PB, Ottino JM, Lueptow RM. Modeling segregation of polydisperse granular materials in developing and transient free-surface flows. AIChE J 2019;65:882—93.
13. Zhou Y, Fan S, Zhu Z, Su S, Hou D, Zhang H, et al. Enabling high-sensitivity calorimetric flow sensor using vanadium dioxide phase-change material with predictable hysteretic behavior. IEEE Trans Electron Devices 2025;72:1360—7.
14. Rasheed HUR, Islam S, Khan Z, Alharbi SO, Alotaibi H, Khan I. Impact of Nanofluid flow over an elongated moving surface with a uniform hydromagnetic field and nonlinear heat reservoir. Complexity 2021;2021:9951162.
15. Durga Bhavani J, Gopal T, Gnanasekar S, Pandiaraj S, Muthu Ramamoorthy MM, Alodhayb AN, et al. Ultrasonic Interferometry and Physiothermal properties of Al2O3/CuO nanofluids. Case Stud Therm Eng 2024;55:104120.
16. Humane PP, Patil VS, Patil AB, Shamshuddin MD. Buongiorno modelled nanoliquid consequence of thermal and solutal convection on the magneto-micropolar fluid inside an inclined porous stretching device. J Nanofluids 2023;12:211—22.
17. Wang F, Saeed AM, Puneeth V, Shah NA, Anwar MS, Geudri K, et al. Heat and mass transfer of Ag—H_2O nano-thin film flowing over a porous medium: a modified Buongiorno's model. Chin J Phys 2023;2056:330—42.
18. Rafique K, Anwar MI, Misiran M, Khan I, Seikh AH, Sherif E-SM, et al. Brownian motion and thermophoretic diffusion effects on micropolar type nanofluid flow with Soret and Dufour impacts over an inclined sheet: Keller-box simulations. Energies 2019;12: 4191.
19. Shahbaz HM, Ahmad I, Raja MAZ, Ilyas H, Nisar KS, Shoaib M. 3D thermally laminated MHD non-Newtonian nanofluids across a stretched sheet: intelligent computing paradigm. J Therm Anal Calorim 2024;150:1—26.
20. Sparrow EM, Yu HS. Local non-similarity thermal boundary-layer solutions. ASME J Heat Transfer 1971;93:328—34.
21. Razzaq R, Farooq U. Non-similar forced convection analysis of Oldroyd B fluid flow over an exponentially stretching surface. Adv Mech Eng 2021;13:1—7.
22. Abdullah A, Ibrahim FS, Chamkha JA. Non-similar solution of unsteady mixed convective flow near the stagnation point of a heated vertical plate in a porous medium saturated with a nanofluid. J Porous Media 2018;21:363—88.
23. Anjum A, Abdul Gaffar S, Kumar S, Peerusab S. Dissipative magneto-thermo-convection of nanofluid past through a semi-infinite vertical surface with ohmic heating. J Appl Comput Mech 2025;11:991—1008.
24. Vedavathi N, Dharmaiah G, Abdul Gaffar S, Venkatadri K. Entropy analysis of nanofluid magnetohydrodynamic convection flow past an inclined surface: a numerical review. Heat Transfer J 2021;50:5996—6021.
25. Farooq U, Razzaq R, Khan MI, Chu YM, Lu DC. Modeling and numerical computation of non-similar forced convective flow of viscous material towards an exponential surface. Int J Mod Phys B 2021;35:2150118.
26. Forchheimer P. Wasserbewegung durch Boden. Z Ver Dtsch Ing 1901;45:1782—8.
27. Muskat M. The flow of homogeneous fluids through porous media. Edwards: Michigan; 1946.
28. Ganesh NV, Abdul Hakeem AK, Ganga B. Darcy—Forchheimer flow of hydromagnetic nanofluid over a stretching/shrinking sheet in a thermally stratified porous medium with second order slip, viscous and ohmic dissipations effects. Ain Shams Eng J 2018;9:939—51.
29. Makinde OD, Khan ZH, Trounev A, Khan WA, Rashid A. Fractional dynamics of entropy generation in unsteady mixed convection of a reacting nanofluid over a slippery permeable plate in Darcy—Forchheimer porous medium. ZAMM-J Appl Math Mech 2024;104:e202400083.
30. Yusuf TA, Mabood F, Prasannakumara BC, Sarris IE. Magneto-bioconvection flow of Williamson nanofluid over an inclined plate with gyrotactic microorganisms and entropy generation. Fluids 2021;6:109.
31. Jawad M, Saeed A, Tassaddiq A, Khan A, Gul T, Kumam P, et al. Insight into the dynamics of second grade hybrid radiative nanofluid flow within the boundary layer subject to Lorentz force. Sci Rep 2021;11:4894.
32. Ge-JiLe H, Nazeer M, Hussain F, Khan MI, Saleem A, SiddiqueGe-JiLe IH, et al. Two-phase flow of MHD Jeffrey fluid with the suspension of tiny metallic particles incorporated with viscous dissipation and porous medium. Adv Mech Eng 2021;13:1—15.
33. Madhu J, Madhukesh JK, Sooppy Nisar K, Sarris I, Prasannakumara BC, Ramesh GK, et al. Influence of waste discharge concentration and quadratic thermal radiation over oblique stagnation point Boger hybrid nanofluid flow across a cylinder. ZAMM-J Appl Math Mech 2025;105:e202300929.
34. Raja MAZ, Shoaib M, Hussain S, Nisar KS, Saeed I. Computational intelligence of Levenberg-Marquardt backpropagation neural networks to study thermal radiation and Hall effects on boundary layer flow past a stretching sheet. Int Commun Heat Mass Transfer 2022;130:105799.
35. Pohlhausen E. Der Wärmeaustausch zwischen festen Körpern und Flüssigkeiten mit kleiner Reibung und kleiner Wärmeleitung. ZAMM-J Appl Math Mech 1921;1:115—21.
36. Ostrach S. An analysis of laminar free-convection flow and heat transfer about a flat plate paralled to the direction of the generating body force; 1953. No. NACA-TR-1111 https://ntrs.nasa.gov/api/citations/19930092147/downloads/19930092147.pdf.
37. Gebhart B, Jaluria Y, Mahajan RL, Sammakia B. Buoyancy induced flows and transport. Washington, DC: Hemisphere; 1988:1—100 pp.

38. Gebhart B, Pera L. The nature of vertical natural convection flows resulting from the combined buoyancy effects of thermal and mass diffusion. Int J Heat Mass Transfer 1971;14:2025—50.
39. Amanulla CH, Nagendra N, Suryanarayana Reddy M. Numerical simulations on magnetohydrodynamic non-Newtonian nanofluid flow over a semi-infinite vertical surface with slip effects. J Nanofluids 2018;7:718—30.
40. Chamkha AJ, Aly AM. MHD free convection flow of a nanofluid past a vertical plate in the presence of heat generation or absorption effects. Chem Eng Commun 2011;198:425—41.
41. Gangadhar K, Kumari MA, Chamkha AJ. EMHD flow of radiative second-grade nanofluid over a Riga plate due to convective heating: revised Buongiorno's nanofluid model. Arabian J Sci Eng 2022;47:8093—103.
42. Narahari M. Unsteady free convection flow past a semi-infinite vertical plate with constant heat flux in water-based nanofluids. IOP Conf Ser Mater Sci Eng 2018;342:012085.
43. Rao VS, Baba LA, Raju RS. Finite element analysis of radiation and mass transfer flow past semi-infinite moving vertical plate with viscous dissipation. J Appl Fluid Mech 2013;6:321—9.
44. Gaffar SA, Prasad VR, Keshava Reddy E. Computational study of Jeffrey's non-Newtonian fluid past a semi-infinite vertical plate with thermal radiation and heat generation/absorption. Ain Shams Eng J 2017;8:277—94.
45. Chamkha AJ, Khaled A-RA. Hydromagnetic combined heat and mass transfer by natural convection from a permeable surface embedded in a fluid-saturated porous medium. Int J Numer Methods Heat Fluid Flow 2000;10:455—77.
46. Anjum A, Kumar DS, Gaffar SA, Peerusab S. Heat and mass transfer in magneto-dissipative Buongiorno nanofluid flow along a semi-infinite plate in a non-Darcy porous medium. Int J Heat Technol 2025;43:583—602.
47. Rosseland S. Astrophysik und atom-theoretischeGrundlagen. Berlin: Springer; 1931.
48. Shamshuddin MD, Mishra SR, Anwar Bég O, Bég TA, Ali K. Computation of radiative Marangoni (thermocapillary) magnetohydrodynamic convection in Cu-water based nanofluid flow from a disk in porous media: smart coating simulation. Heat Transfer 2021;50:1931—50.
49. Uddin MJ, Khan WA, Anwar Bég O, Ismail AIM. Non-similar solution of g-jitter induced unsteady magnetohydrodynamic radiative slip flow of nanofluid. Appl Sci 2020;10:1420.
50. Ketchate CGN, Kapen PT, Fokwa D, Tchuen G. Stability analysis of mixed convection in a porous horizontal channel filled with a Newtonian Al2O3/water nanofluid in presence of magnetic field and thermal radiation. Chin J Phys 2022;79:514—30.
51. Keller HB. Numerical methods in boundary-layer theory. Annu Rev Fluid Mech 1978;10:417—33.
52. Abdul Gaffar S, Anwar Bég O, Ramachandra Prasad V, Hidayathulla Khan BM, Kadir A. Computation of Eyring-Powell micropolar convective boundary layer flow from an inverted non-isothermal cone: thermal polymer coating simulation. Comput Therm Sci 2020;12:329—44.
53. Gaffar SA, Anwar Bég O, Kuharat S, Bég TA. Computation of hydromagnetic tangent hyperbolic non-Newtonian flow from a rotating non-isothermal cone to a non-Darcy porous medium with thermal radiative flux. Phys Open 2024;19:100216.
54. Reddy R, Abdul Gaffar S. Chemical reaction and viscous dissipative effects on Buongiorno's nanofluid model past an inclined plane: a numerical investigation. Int J Appl Comput Math 2024;10:81.
55. Bég OA. Numerical methods for multi-physical magnetohydrodynamics. J Magnetohydrodyn Plasma Res 2013;18:93.
56. Anjum A, Abdul Gaffar S, Sateesh Kumar D, Anwar Bég O, Peerusab S. Non-similar Keller box analysis of magnetically radiative Buongiorno's nanofluid flows past a stretching surface. J Nav Architect Mar Eng 2024;21:127—53.